A spectral/hp element depth-integrated model for nonlinear wave-body interaction

Umberto Bosi, Allan P Engsig-Karup, Claes Eskilsson, Mario Ricchiuto

A spectral/*hp* element depth-integrated model for nonlinear wave-body interaction

Umberto Bosi[a], Allan P. Engsig-Karup[b,c], Claes Eskilsson[d,e], Mario Ricchiuto[a,*]

[a]*Team CARDAMOM, INRIA Bordeaux Sud-Ouest, 200 avenue de la vieille tour, 33405 Talence cedex, France*
[b]*Department of Applied Mathematics and Computer Science, Technical University of Denmark, 2800 Kgs. Lyngby, Denmark*
[c]*Center for Energy Resources Engineering (CERE), Technical University of Denmark, 2800 Kgs. Lyngby, Denmark*
[d]*Division Safety & Transport, RISE Research Institutes of Sweden, 50115 Borås, Sweden*
[e]*Department of Civil Engineering, Aalborg University, 9220 Aalborg Ø, Denmark*

Abstract

We present a depth-integrated Boussinesq model for the efficient simulation of nonlinear wave-body interaction. The model exploits a 'unified' Boussinesq framework, i.e. the fluid under the body is also treated with the depth-integrated approach. The unified Boussinesq approach was initially proposed by Jiang [26] and recently analysed by Lannes [29]. The choice of Boussinesq-type equations removes the vertical dimension of the problem, resulting in a wave-body model with adequate precision for weakly nonlinear and dispersive waves expressed in horizontal dimensions only. The framework involves the coupling of two different domains with different flow characteristics. Inside each domain, the continuous spectral/*hp* element method is used to solve the appropriate flow model since it allows to achieve high-order, possibly exponential, convergence for non-breaking waves. Flux-based conditions for the domain coupling are used, following the recipes provided by the discontinuous Galerkin framework. The main contribution of this work is the inclusion of floating surface-piercing bodies in the conventional depth-integrated Boussinesq framework and the use of a spectral/*hp* element method for high-order accurate numerical discretization in space. The model is verified using manufactured solutions and validated against published results for wave-body interaction. The model is shown to have excellent accuracy and is relevant for applications of waves interacting with wave energy devices.

Keywords: nonlinear and dispersive waves, wave-body interaction, Boussinesq equations, spectral/*hp* element method, discontinuous Galerkin method, domain decomposition

1. Introduction

Wave models based on depth-integrated Boussinesq-type wave equations, e.g. [41, 2, 33], are standard engineering tools for predicting nonlinear wave propagation and transformation in coastal areas. Boussinesq-type models are computationally efficient due to the elimination of the vertical dimension of the problem, as well as avoiding the problem of a time-dependent computational domain caused by the moving free surface boundary condition. However, by its nature, the depth-integrated approach makes truncated surface-piercing bodies troublesome to handle. In order to include truncated bodies in depth-integrated hydrodynamic models methods such as pressure patches [17], porosity layers [38] and slender ship approximations [7] have been used. None of these approaches includes the actual body in the discretization. The exception is the work of Jiang [26] on the 'unified' Boussinesq model. Jiang decomposed the domain into a free-surface domain and a body domain. Importantly, Jiang modelled also the domain under the

*Corresponding author. E-mail: mario.ricchiuto@inria.fr

body with a depth-integrated approach – hence the term 'unified'. Recently, a similar setting was rigorously analyzed by Lannes [29]. Lannes extended the work of John [27] to include nonlinear contributions and derived semi-analytic nonlinear solutions for the wave-body problem using the nonlinear shallow water equations. Thus, the study of Lannes mainly kept within the traditional shallow water limit. The 'roofed', congested shallow water flows are discussed also in [23].

In this study we propose a depth-integrated unified Boussinesq model for nonlinear wave-body interaction based on the approach introduced by Jiang [26]. Adapting the original idea in terms of governing equations and discretizations, we employ a spectral/*hp* finite element method for the simulation of nonlinear and dispersive waves interacting with fixed and heaving bodies. In particular, we employ the continuous spectral/*hp* element method [28] inside each domain, and implement flux-based coupling conditions between domains in line with the discontinuous Galerkin spectral/*hp* element method [8]. This results in a new efficient and accurate model that simulates the wave propagation and the nonlinear interaction of waves with bodies. However, as all models based on Boussinesq-type equations, the model is limited to shallow and intermediate depth regimes. The use of spectral/*hp* elements give support for the use of adaptive meshes for geometric flexibility and high-order accurate approximations makes the scheme computationally efficient. High-order finite element methods for depth-integrated wave models have been presented in [20, 21, 15, 13, 11, 44].

The current study, which expands and improves the concepts introduced in [18], presents the underlying formulation of the method as well as verification and validation of the numerical model. Although the model is not limited to applications in marine renewable energy, the rationale for developing a medium fidelity wave-body model is found in the present state of modelling wave energy converters (WECs). Today the industry standard description of the interaction between waves and WECs is based on models solving the Cummins equation [9] using hydrodynamic coefficients computed from linear potential flow (LPF). The LPF models are based on the small-amplitude assumption and they are widely used for their simplicity and efficiency, e.g. see [34]. Thus, the LFP models can not account for nonlinear hydrodynamic effects which are of importance especially for survival cases as well as for WECs operating inside the resonance region. The LPF models over-predict the power production in the resonance region unless drag coefficients are calibrated. Moreover, WEC farms are often planned to be placed in near-shore regions where it is unlikely to have a flat seabed. Hence, waves are expected to exhibit nonlinear dynamics, as steepening and energy transfer between harmonics. More recently, Reynolds Averaged Navier-Stokes (RANS) simulations have been employed for point absorber WECs, e.g. [47, 40, 3]. RANS is a complete and accurate model with respect to nonlinear phenomena but computationally very costly. For example, a simulation with a full sea state for a WEC may require as much as 150 000 CPU hours per simulation [19]. At present RANS models are therefore unsuited for the optimization of single devices, not to mention energy farms. In shallow to intermediate waters, Boussinesq-type models as the one proposed here, are an intermediate way between the efficient but too simple linear model and the complete but too expensive RANS model.

The paper is structured as follows. In section 1 we outline the governing equations based on the enhanced Boussinesq-type equations of Madsen and Sørensen (MS) [33]. Further, the fluid under the body is defined and it is illustrated that high-order terms are negligible in the body domain under the assumption of no rotational degrees of freedom. The numerical discretisation in space and time is described in section 3. In particular we discuss the coupling between free surface domain and the body constrained domain. In section 4 first the model coupling is verified by means of the method of manufactured solutions (sections 4.1 – 4.4). Then, the model is validated against test cases found in literature (sections 4.6 – 4.7). A heaving box test is presented in section 4.8 and the results from the Boussinesq model is compared to LPF and RANS simulations. A proof-of-concept highlighting the flexibility of the framework with multiple bodies interacting with weakly nonlinear incoming waves is demonstrated in section 4.9. Finally, the the conclusions are found in section 5.

2. Governing Equation

We present here the governing equations of the nonlinear wave-body interaction problem. In the proposed unified Boussinesq approach, the domain is decomposed into an outer free surface sub-domain Ω_w and a inner sub-domain Ω_b that represents the area under the structure, as shown in figure 1. The present work is limited to straight-sided body interfaces that are assumed vertical at the wave-body intersection. Additionally, only heave motion is considered here for simplicity. Boussinesq-type models for free surface flows can be derived from the fully nonlinear potential

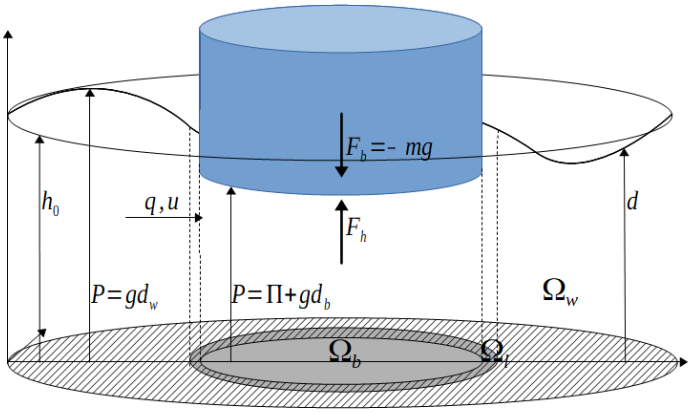

Figure 1: 3D Layout of the problem describing the nonlinear wave-body interaction in a domain decomposition framework.

equations for an incompressible, irrotational and non-viscous fluid by expanding the velocity potential in terms of the vertical coordinate and integrating the Laplace equation over the water depth. Let A_0, h_0 and λ_0 denote the characteristic wave amplitude, characteristic still water depth and characteristic wave length. Boussinesq-type equations are then obtained as an asymptotic approximation in terms of nonlinearity ($\varepsilon = A_0/h_0$) and dispersion ($\mu = 2\pi h_0/\lambda_0$). These asymptotic and depth integrated models have the advantage of reducing the original problem to a lower-dimensional one ($\mathbb{R}^d \to \mathbb{R}^{d-1}$), but it comes with an application window that depends on the approximation order of nonlinearity and dispersion assumed in the derivation procedure [32].

2.1. Free surface domain

The shallow water approximation is relevant only for very long waves and, in general, when the dispersion parameter κh_0 is less than $\approx \pi/20$, with $\kappa = 2\pi/\lambda_0$ the wavenumber and h_0 the still water depth. To account for the dispersive effects taking place for shorter waves, we consider Boussinesq-type models that includes weakly nonlinear and dispersive effects. In this work we will employ the enhanced Boussinesq-type model proposed by Madsen and Sørensen (MS) [33] which can be written (assuming constant bathymetry) as

$$d_t + \nabla \cdot \boldsymbol{q} = 0\,, \tag{1a}$$

$$\boldsymbol{q}_t + \nabla \cdot (\boldsymbol{u} \otimes \boldsymbol{q}) + d\nabla P = Bh_0^2 \nabla(\nabla \cdot \boldsymbol{q}_t) - \alpha_{MS} h_0^3 \nabla(\Delta P)\,, \tag{1b}$$

where $d(\boldsymbol{x}, t)$ is the water depth measured as the height of the water column and $\boldsymbol{q}(\boldsymbol{x}, t)$ is the mass flux. The mass flux is simply $\boldsymbol{q} = d\boldsymbol{u}$ in which $\boldsymbol{u}(\boldsymbol{x}, t)$ is the depth-averaged horizontal velocity. The acceleration of gravity is denoted by g. Please note the use of horizontal gradient (∇) and Laplace (Δ) operators. In eq. (1b) the total specific pressure is defined as

$$P(\boldsymbol{x}, t) = gd(\boldsymbol{x}, t) + \Pi(\boldsymbol{x}, t). \tag{2}$$

Here $\Pi(\boldsymbol{x}, t)$ represents the pressure at the free surface and it is equal to the atmospheric pressure. It is custom to set the atmospheric pressure above the free surface to zero. The free parameters α_{MS} and B are used to optimize the linear dispersion relation of the system [42]. The parameters are defined in the literature as $\alpha_{MS} = 1/15$ and $B = 1/3 + \alpha_{MS}$ [42] to give an application window of $\kappa h_0 \approx \pi$, for which the error in linear phase velocity is less than 5% with respect to the exact phase velocity of the Euler incompressible flow [22]. Note that varying the two parameters we can recover other long wave equations. Setting $\alpha_{MS} = B = 0$ we recover the standard nonlinear hydrostatic shallow water (NSW) model. The NSW model is valid only for hydrostatic pressure.

2.2. Body model

As shown in [29], eq. (1) with $\alpha_{MS} = 0$ is also valid in the domain below the body Ω_b. However, as shown in [32], under the standard Boussinesq assumption we can derive the MS model valid for every α_{MS}. In the inner domain, Π represents the pressure on the body surface, which is a priori neither constant nor known. Further, d still denotes the elevation of the water column but is now restrained by the body geometry and is known. However, in the inner domain we can prove the following result:

Proposition 1. *Under the standard assumption of the Boussinesq theory of*

$$\mu^4 \ll 1, \quad \mu^2 \approx \varepsilon. \tag{3}$$

and in absence of pitch, roll and yaw, all terms accounting for higher-order dispersive effects in the inner domain are negligible, within the classical Boussinesq truncation of $O(\mu^4, \mu^2\varepsilon, \varepsilon^2)$.

Proof. Introducing the inner domain nondimensional variables

$$\begin{aligned} &\tilde{t} = \mu\frac{\sqrt{gh_0}}{h_0}t, \quad \tilde{\boldsymbol{x}} = \frac{\mu}{h_0}\boldsymbol{x}, \quad \tilde{z} = \frac{z}{h_0}, \quad \tilde{h}(\tilde{\boldsymbol{x}}) = \frac{h(x)}{h_0}, \quad \tilde{\eta}(\tilde{\boldsymbol{x}}, \tilde{t}) = \frac{\eta(\boldsymbol{x}, t)}{\varepsilon h_0}, \quad \tilde{d}(\tilde{\boldsymbol{x}}, \tilde{t}) = \varepsilon\tilde{\eta}(\tilde{\boldsymbol{x}}, \tilde{t}) + \tilde{h} = \frac{d(\boldsymbol{x}, t)}{h_0}, \\ &\tilde{\boldsymbol{u}} = \frac{1}{\varepsilon\sqrt{gh_0}}\boldsymbol{u}, \quad \tilde{\boldsymbol{q}} = \tilde{d}\tilde{\boldsymbol{u}}, \quad \tilde{w} = \frac{\mu}{\varepsilon\sqrt{gh_0}}w, \quad \tilde{P} = \frac{1}{\varepsilon\rho_w g h_0}P, \quad \tilde{B} = \frac{B}{h_0^2}, \quad \tilde{\alpha}_{MS} = \frac{\alpha_{MS}}{h_0^3} \end{aligned} \tag{4}$$

where η is the instantaneous wave elevation and w the vertical velocity component. The nondimensional MS problem reads

$$\tilde{d}_t + \nabla\cdot\tilde{\boldsymbol{q}} = O(\mu^4, \varepsilon\mu^2, \varepsilon^2), \tag{5a}$$

$$\tilde{\boldsymbol{q}}_t - \mu^2\tilde{B}\nabla(\nabla\cdot\tilde{\boldsymbol{q}}_t) + \varepsilon\nabla\cdot(\tilde{u}\otimes\tilde{q}) + \rho_w\tilde{d}\nabla\tilde{P} + \tilde{\alpha}_{MS}\mu^2\rho_w\nabla(\Delta\tilde{P}) = O(\mu^4, \varepsilon\mu^2, \varepsilon^2). \tag{5b}$$

From the mass eq. (5)

$$\nabla\tilde{d}_{tt} + \nabla(\nabla\cdot\tilde{\boldsymbol{q}}_t) = 0, \tag{6}$$

but in the inner domain the water elevation is at the bottom of the body, therefore d represent the body geometry and $\nabla d_{tt} = 0$ as it is the derivative of a constant value in space and the dispersion term is zero. To demonstrate that the term $\nabla(\Delta P) = 0$, consider the nondimensional momentum eq. (5b) under the Boussinesq assumption eq. (3):

$$\tilde{\boldsymbol{q}}_t + \rho_w\tilde{d}\nabla\tilde{P} = O(\mu^4, \varepsilon\mu^2, \varepsilon^2), \tag{7}$$

the variable $\tilde{d} = \tilde{h}_0 + O(\varepsilon)$ so we simplify eq. (7) to express it in the form

$$\tilde{\boldsymbol{q}}_t + \rho_w\tilde{h}_0\nabla\tilde{P} = O(\mu^4, \varepsilon\mu^2, \varepsilon^2). \tag{8}$$

Taking the gradient of the divergence of eq. (8)

$$\nabla(\nabla\cdot\tilde{\boldsymbol{q}})_t + \rho_w\nabla(\nabla\cdot(\tilde{h}_0\nabla\tilde{P})) = O(\mu^4, \varepsilon\mu^2, \varepsilon^2), \tag{9}$$

for a constant bathymethry, $\tilde{h}_0$ can be moved out the derivation

$$\nabla(\nabla\cdot\tilde{\boldsymbol{q}}_t) + \rho_w\tilde{h}_0\nabla(\Delta\tilde{P}) = O(\mu^4, \varepsilon\mu^2, \varepsilon^2), \tag{10}$$

but we know that $\nabla(\nabla\cdot\tilde{\boldsymbol{q}}_t) = 0$, which proves that $\nabla(\Delta\tilde{P})$ is within the asymptotic error and within this assumption leads to the conclusion that this term is negligible. □

Thanks to proposition 1, it is possible to use the NSW model in the inner domain. The total pressure P is evaluated by taking the divergence of eq. (1b) with $\alpha_{MS} = B = 0$

$$-\nabla\cdot(d\nabla P) = \nabla\cdot\boldsymbol{q}_t + \nabla\cdot(\nabla\cdot(\boldsymbol{u}\otimes\boldsymbol{q})). \tag{11}$$

Introducing the vertical acceleration $a = d_{tt}$, and using the continuity eq. (1a) we have

$$a + (\nabla\cdot\boldsymbol{q})_t = 0, \tag{12}$$

and assuming that all variables are continuous, we can change the order of the space and time derivative

$$a = -\nabla\cdot(\boldsymbol{q}_t). \tag{13}$$

Combining eqs. (11) and (13), we can show that in both the inner and outer domains the total pressure satisfies the following equation

$$-\nabla\cdot(d\nabla P) = -a + \nabla\cdot(\nabla\cdot(\boldsymbol{u}\otimes\boldsymbol{q})). \tag{14}$$

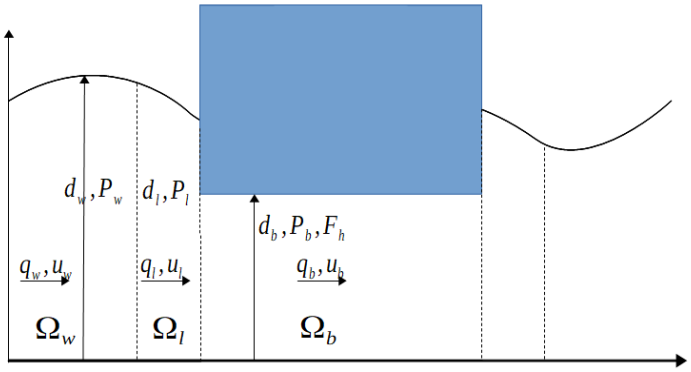

Figure 2: 1D Layout of the problem describing the nonlinear wave-body interaction in a domain decomposition framework.

2.3. Boundary and coupling conditions

The coupling conditions between hydrostatic free surface and body domains have been presented in [29]. The transmission/coupling conditions between the fully non-hydrostatic free surface domain and the submerged domain under the body have not been rigorously formulated in the nonlinear case [29, 30]. Thus, to reduce the complexity of this coupling we have decided to handle them numerically introducing an intermediate (thin) hydrostatic coupling layer (denoted by Ω_l) in which the flow is described by the NSW equations (eqs. (21a) and (21b) with $\alpha_{MS} = B = 0$). The role of this layer is to introduce a first transition between non-hydrostatic and hydrostatic conditions, and a second between free surface and constrained flow. Note that the equations of the coupling layer can be found setting the dispersive term D in eq. (25b) to zero.

The flow in separated domains is coupled through the mass flux $\boldsymbol{q}$ and the total pressure P. At the interface between the body and free surface domains, $(x_{li}, y_{li}) \in \Omega_l \cap \Omega_b$ the coupling conditions at the waterline read

$$\boldsymbol{q}_l(x_{li}, y_{li}) = \boldsymbol{q}_b(x_{li}, y_{li}), \tag{15}$$

$$P_l(x_{li}, y_{li}) = P_b(x_{li}, y_{li}). \tag{16}$$

where $(\boldsymbol{q}_l, P_l) \in \Omega_l$ and $(\boldsymbol{q}_b, P_b) \in \Omega_b$. Note that the pressure coupling condition eq. (16) can be expanded and written also as

$$g d_l(x_{li}, y_{li}) = g d_b(x_{li}, y_{li}) + \Pi_b(x_{li}, y_{li}). \tag{17}$$

When coupling the two free surface domains, at $(x_{wl}, y_{wl}) \in \Omega_w \cap \Omega_l$, $\Pi(x_{wl}, y_{wl})$ is zero and the condition states that the wave elevation and the flow must be equal through the interface

$$\begin{aligned} d_w(x_{wi}, y_{wi}) &= d_l(x_{wl}, y_{wl}); \\ q_w(x_{wl}, y_{wl}) &= q_l(x_{wl}, y_{wl}). \end{aligned} \tag{18}$$

On the external boundaries of the outer domains (on the far field), we impose the absorption of the wave, thus

$$\begin{aligned} d_w|_{\pm\infty} &= h_0; \\ \boldsymbol{q}_w|_{\pm\infty} &= 0. \end{aligned} \tag{19}$$

2.4. Complete model

We introduce the linear operators

$$\mathcal{L}_B(\cdot) = (1 - B h_0^2 \nabla(\nabla\cdot)), \qquad \mathcal{B}_d^{\alpha}(\cdot) = d\nabla(1 + \alpha_{MS} h_0^2 \Delta). \tag{20}$$

Note that the operator $\mathcal{B}_d^\alpha(\cdot)$ contains also the high order component dependent on d. This is possible since the still water depth h_0 and the instant elevation d are of the same order of approximation and they can be substituted one with the other (see in proposition 1).

We have a set of three equations which have to be satisfied

$$P_t + g\nabla\cdot\boldsymbol{q} = 0\,, \qquad \boldsymbol{x}\in\Omega_l\cup\Omega_w; \tag{21a}$$
$$\mathcal{L}_B\boldsymbol{q}_t + \nabla\cdot(\boldsymbol{u}\otimes\boldsymbol{q}) + \mathcal{B}_d^\alpha P = 0\,, \tag{21b}$$
$$(\alpha_{MS}, B) = \begin{cases}(1/15, 1/3+\alpha_{MS}), & x\in\Omega_w,\\ (0,0)\,, & x\in\Omega_l.\end{cases} \tag{21c}$$

$$d_t + \nabla\cdot\boldsymbol{q} = 0\,, \in\Omega_b; \tag{22a}$$
$$-\nabla\cdot(d\nabla P) = -a + \nabla\cdot(\nabla\cdot(\boldsymbol{u}\otimes\boldsymbol{q})), \tag{22b}$$
$$\boldsymbol{q}_t + \nabla\cdot(\boldsymbol{u}\otimes\boldsymbol{q}) + d\nabla P = 0\,, \tag{22c}$$

where the mass eq. (21a) has been multiplied by g such that all the models are solved in (P, q) formulation. The main difference between the free surface domain and the body domain is that in Ω_w the total pressure and the free surface elevation are readily obtained by eq. (21a), automatically satisfying eq. (21b) (which should include high order terms). On the other hand, in the inner domain Ω_b, the relation (22a) acts as a constraint on the flux divergence, exactly as in incompressible flow. In particular, this is where the coupling with the dynamics of the body appear. For a purely heaving body, the vertical acceleration will be determined by the application of Newton's second law to the body

$$m_b a = -m_b g + F_h\,. \tag{23}$$

The hydrodynamic force F_h is evaluated integrating the hydrodynamic pressure Π over the body bottom

$$F_h = \rho_w\int_{\Omega_b}\Pi\boldsymbol{n}_z^b d\boldsymbol{x}\,, \tag{24}$$

where ρ_w is the water density, m_b the mass of the body and $\boldsymbol{n}_z^b$ is the vertical component of the inward normal vector to the surface. Eq. (23) is added to the final NSW system to account for the movement of the body caused by the wave-body interaction.

3. Numerical Model

The focus of this paper is to model wave and wave-body interaction in 2D (vertical plane) using a coupled 1D system of PDEs. As the domains will be coupled following a DG-FEM approach the equations are re-written as a first order system by introducing auxiliary variables. In the free surface domain, unless otherwise stated, we will solve the 1D MS eqs.(21)

$$P_t + gq_x = 0\,; \tag{25a}$$
$$q_t + uq_x + dP_x = D\,; \tag{25b}$$
$$D = Bh_0^2G_x + \alpha_{MS}h_0^2dF_x\,, \qquad x\in\Omega_w; \tag{25c}$$
$$G - q_{xt} = 0\,; \tag{25d}$$
$$F - N_x = 0\,; \tag{25e}$$
$$N - P_x = 0. \tag{25f}$$

where we have multiplied the mass eq. (25) by g such that we can use the same set of variables (P, q), through all the domains. The transition domain ($c\in\Omega_l$) is given by eq. (25) with $D\equiv 0$. In the body domain we solve the non dispersive 1D NSW system (22)

$$q_t + (uq)_x + dP_x = 0\,; \tag{26a}$$
$$-w_x = -a + k_x\,, \qquad x\in\Omega_b; \tag{26b}$$
$$w - dP_x = 0\,; \tag{26c}$$
$$k - (qu)_x = 0. \tag{26d}$$

3.1. Spatial Discretization

Consider the domain Ω, which can represent the any of the domains presented, and a test function φ defined in the discrete space $\mathcal{V}^P$

$$\mathcal{V}^p = \left\{ \varphi_i \in L^2(\Omega) : \varphi_i|_\Omega \in \mathcal{P}^p \right\}, \tag{27}$$

where $\mathcal{P}^p$ is the space of polynomials of degree at most p. We propose a spectral/*hp* element approach to discretize in space the models presented in section 1. Following a DG-FEM type recipe based on double integration by parts on each sub-domain [10, 24], we multiply the eqs. (25) and (26) by φ and integrate in each domain to obtain the weak form. However, the systems present non-conservative products, namely the dP_x terms, which are not continuous over the boundaries from the free surface domains to the body one. The non-conservative products are handled by introducing penalty terms consistent with a local linearization of the quasi-linear form of the system [10, 6, 37]. The weak form of the free surface equations reads:

$$\int_{\Omega_w} \varphi_i P_t dx + g \int_{\Omega_w} \varphi_i q_x dx + g \int_{\partial\Omega_w \cap \partial\Omega_l} \varphi_i [q] \boldsymbol{n} dx = 0, \tag{28a}$$

$$\int_{\Omega_w} \varphi_i q_t dx + \int_{\Omega_w} \varphi_i (qu)_x dx + \int_{\partial\Omega_w \cap \partial\Omega_l} \varphi_i [qu] \boldsymbol{n} dx + \int_{\Omega_w} \varphi_i dP_x dx + \int_{\partial\Omega_w \cap \partial\Omega_l} \varphi_i \hat{d} [P] \boldsymbol{n} dx = \int_{\Omega_w} \varphi_i D dx, \tag{28b}$$

$$\int_{\Omega_w} \varphi_i D dx = B h_0^2 \left(\int_{\Omega_w} \varphi_i G_x dx + \int_{\partial\Omega_w \cap \partial\Omega_l} \varphi_i [G] \boldsymbol{n} dx \right) + \alpha_{MS} h_0^2 \left(\int_{\Omega_w} \varphi_i dF_x dx + \int_{\partial\Omega_w \cap \partial\Omega_l} \varphi_i \hat{d} [F] \boldsymbol{n} dx \right), \tag{28c}$$

$$\int_{\Omega_w} \varphi_i G dx - \int_{\Omega_w} \varphi_i q_{xt} - \int_{\partial\Omega_w \cap \partial\Omega_l} \varphi_i [q_t] \boldsymbol{n} dx = 0, \tag{28d}$$

$$\int_{\Omega_w} \varphi F - \int_{\Omega_w} \varphi_i N_x - \int_{\partial\Omega_w \cap \partial\Omega_l} \varphi_i [N] \boldsymbol{n} dx = 0, \tag{28e}$$

$$\int_{\Omega_w} \varphi_i N - \int_{\Omega_w} \varphi_i P_x - \int_{\partial\Omega_w \cap \partial\Omega_l} \varphi_i [P] \boldsymbol{n} dx = 0. \tag{28f}$$

where $\boldsymbol{n}$ represents the outward pointing normal vector. In general, the integral boundary terms are in the form

$$[f] = \hat{f} - f^- \tag{29}$$

where $\hat{f}$ represent a numerical flux through the boundary interface and f^- the value of the function on the boundary for x inside the domain. Note that the numerical flux between the domains is often based on an approximate Riemann solver for the advective parts [20] and a local discontinuous Galerkin type [46] or hybridizeable discontinuous Galerkin [44] for the higher-order terms. Here we have used simple central fluxes

$$\hat{f} = \frac{1}{2} \left(f^+ + f^- \right). \tag{30}$$

Substituting in eq. (29), we obtain the jumps between the domains for first derivative terms

$$[f] = \frac{1}{2} \left(f^+ - f^- \right), \tag{31}$$

where u^+ is the values on the boundary in the neighbor domain. The coefficient multiplying non conservative terms is treated taking the average value of the depth on the two side of the boundary

$$\hat{d} = \frac{d^+ + d^-}{2}. \tag{32}$$

This simple choice allows to recover the conservative form in the hydrostatic free surface region, as we have exactly that

$$\hat{d}[d] = \frac{\hat{d}^2}{2} - \left(\frac{d^2}{2} \right)^- . \tag{33}$$

In the same manner, we evaluate the weak formulation in the body domain

$$\int_{\Omega_b} \varphi_i q_t dx + \int_{\Omega_b} \varphi_i (qu)_x dx + \int_{\partial\Omega_b \cap \partial\Omega_l} \varphi_i [qu] \boldsymbol{n} dx + \int_{\Omega_b} \varphi_i dP_x dx + \int_{\partial\Omega_b \cap \partial\Omega_l} \varphi_i \hat{d}[P] \boldsymbol{n} dx = 0, \tag{34a}$$

$$- \int_{\Omega_b} \varphi_i w_x dx \int_{\partial\Omega_b \cap \partial\Omega_l} \varphi_i [w] \boldsymbol{n} dx = - \int_{\Omega_b} \varphi_i a dx + \int_{\Omega_b} \varphi_i k_x dx \int_{\partial\Omega_b \cap \partial\Omega_l} \varphi_i [k] \boldsymbol{n} dx, \tag{34b}$$

$$\int_{\Omega_b} \varphi_i w - \int_{\Omega_b} \varphi_i dP_x - \int_{\partial\Omega_b \cap \partial\Omega_l} \varphi_i \hat{d}[k] \boldsymbol{n} dx = 0, \tag{34c}$$

$$\int_{\Omega_b} \varphi_i k - \int_{\Omega_b} \varphi_i (qu)_x - \int_{\partial\Omega_b \cap \partial\Omega_l} \varphi_i [qu] \boldsymbol{n} dx = 0, \tag{34d}$$

with the force balance on the body surface

$$m_b a = -m_b g + \rho_w \int_{\Omega_b} \Pi dx. \tag{35}$$

Definition 1. *We define as hydrostatic equilibrium, the state*

$$(\bar{d}_{w,l}, \bar{d}_b(x), \bar{P}, \bar{q}, \bar{u}, \bar{a}) = (h_0, d_b(x), g h_0, 0, 0, 0), \tag{36}$$

with $d_b(x)$ and h_0 equilibrium depths under the body and in the free surface regions, linked by the hydrostatic equilibrium relation

$$\frac{m_b}{\rho_w} = \int_{\Omega_b} (h_0 - \bar{d}_b(x)) dx. \tag{37}$$

Proposition 2. *The variational formulations eqs.* (28)*,* (34) *are exactly well balanced: the hydrostatic equilibrium eq.* (36) *is an exact solution of the weak form.*

Proof. The main idea of the proof is to show that replacing the steady state in eq. (36) with condition of eq. (37) in the variational form, results in an identity 0=0. As in eq. (36) all the fluxes and velocities are zero, only the terms related to variations of the total pressure P may contribute to to form.We look at each domain separately.

In the outer domain, by definition $\bar{P}_w = g h_0$ and constant in time. So eqs. (28b)-(28f) lead to $N = F = G = D = 0$. The only term which may remain is the one related to the jump of the total pressure between the outer domain and the coupling layer $\int_{\partial\Omega_w \cap \partial\Omega_l} \varphi_i [\cdot] \boldsymbol{n} dx$. However, as in the latter we also have by definition $\bar{P}_l = g h_0$, these jumps are also identically zero.

In the coupling layer $\bar{P}_l = g h_0$ and it is constant in time, so only terms which may give a non-zero contribution are the one related to total pressure jump with the below body region $\int_{\partial\Omega_l \cap \partial\Omega_b} \varphi_i [\cdot] \boldsymbol{n} dx$. If $\bar{P}_b = g h_0$ too, then the proof is achieved. This is easily seen from the force balance on the body at steady state. In particular, substituting the hydrostatic equilibrium eq. (36) in the force balance eq. (35), using eq. (37), one gets to the condition

$$0 = \rho_w \int_{\Omega_w} \bar{P}_b dx - \rho_w \int_{\Omega_w} g h_0 dx, \tag{38}$$

which must be true independently on the body shape and on the domain size. In particular, this is true if $\bar{P}_b = g h_0$ throughout the inner domain, which also satisfies the auxiliary relations eqs. (34c) and (34d). □

To obtain a fully discrete model, we now replace the unknowns with a spectral/*hp* element approximation spanned by high-order polynomial basis functions ψ_j

$$f(x,t) = \sum_{j=0}^{N_{dof}} \psi_j(x) f_j(t), \tag{39}$$

$f_j(t)$ are expansion coefficient of f in the domain Ω and N_{dof} the number of degrees of freedom in the domain considered. Following the standard Galerkin formulation the test function and the interpolation polynomial are the

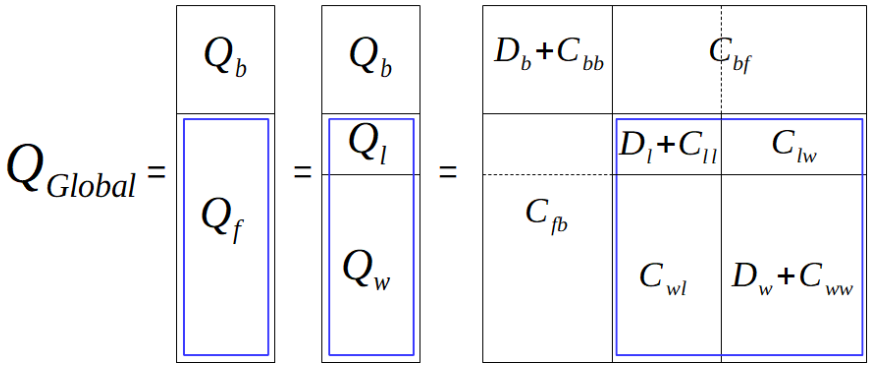

Figure 3: Representation of the global first derivative matrix

same, i.e. $\varphi \in \text{span}\{\psi_j\}$. In this study we use the abscissas of the Gauss-Legendre-Lobatto quadrature rule to define the nodal Lagrange polynomials [28]. We introduce then the mass and differentiation matrices, defined as

$$\boldsymbol{M}_{ij} \equiv \int_{\Omega_\gamma} \psi_i \psi_j dx, \tag{40a}$$

$$\boldsymbol{Q}_{ij} \equiv \int_{\Omega_\gamma} \psi_i (\psi_j)_x dx + 0.5\left(\psi_1\psi_1|_{\in\Omega_\gamma} - \psi_1\psi_N|_{\in\Omega_{\gamma^+}}\right) - 0.5\left(\psi_N\psi_N|_{\in\Omega_\gamma} - \psi_N\psi_1|_{\in\Omega_{\gamma^+}}\right), \tag{40b}$$

$$\tilde{\boldsymbol{Q}}_{ij} \equiv \int_{\Omega_\gamma} \psi_i d_j (\psi_j)_x dx + 0.5\langle d\rangle_{\gamma^+,\gamma}\left(\psi_1\psi_1|_{\in\Omega_\gamma} - \psi_1\psi_N|_{\in\Omega_{\gamma^+}}\right) - 0.5\langle d\rangle_{\gamma,\gamma^+}\left(\psi_N\psi_N|_{\in\Omega_\gamma} - \psi_N\psi_1|_{\in\Omega_{\gamma^+}}\right), \tag{40c}$$

having defined Ω_γ the domain of interest, Ω_{γ^+} the domains at its right and left. The first derivative coupled matrices $\boldsymbol{Q}$ and $\tilde{\boldsymbol{Q}}$ can be written as

$$\begin{aligned} \boldsymbol{Q}_\gamma &= \boldsymbol{D}_\gamma + \boldsymbol{C}_{\gamma\gamma} + \boldsymbol{C}_{\gamma\gamma^+} \\ \tilde{\boldsymbol{Q}}_\gamma &= \tilde{\boldsymbol{D}}_\gamma + \tilde{\boldsymbol{C}}_{\gamma\gamma} + \tilde{\boldsymbol{C}}_{\gamma\gamma^+}. \end{aligned} \tag{41}$$

In particular $\boldsymbol{D}_\gamma$ and $\tilde{\boldsymbol{D}}_\gamma$ are the first derivative matrices internal to the domain Ω_γ, $\boldsymbol{C}_{\gamma\gamma}$ and $\tilde{\boldsymbol{C}_{\gamma\gamma}}$ are the coupling matrices internal to the domain Ω_γ and $\boldsymbol{C}_{\gamma\gamma^+}$ and $\tilde{\boldsymbol{C}}_{\gamma\gamma^+}$ are the coupling matrices that evaluate the value in the domain Ω_{γ^+} on the interface $\partial\Omega_\gamma \cap \partial\Omega_{\gamma^+}$. A representation of the global $\boldsymbol{Q}$ matrix is presented in figure 3 as an example. The semi-discrete formulation of eq. (22) reads

$$\boldsymbol{M}_{w,l} P_t + g\boldsymbol{Q}_{w,l} q = 0\,, \qquad x \in \Omega_w \cup \Omega_l, \tag{42a}$$

$$\boldsymbol{L}_B q_t + \boldsymbol{Q}_w(uq) + \boldsymbol{B}_d^\alpha P = 0\,, \qquad x \in \Omega_w, \tag{42b}$$

$$\boldsymbol{M}_{l,b} q_t + \boldsymbol{Q}_{l,b}(uq) + \tilde{\boldsymbol{Q}}_{l,b} P = 0\,, \qquad x \in \Omega_l \cup \Omega_b, \tag{42c}$$

$$-\boldsymbol{Q}_b \boldsymbol{M}_b^{-1} \tilde{\boldsymbol{Q}}_b P = -\boldsymbol{M}_b \mathbb{1} a + \boldsymbol{Q}_b \boldsymbol{M}_b^{-1} \boldsymbol{Q}_b(uq)\,, \qquad x \in \Omega_b. \tag{42d}$$

where $\mathbb{1}$, in eq. (42d), represents a vector of ones as the acceleration is a scalar variable. The subscripts $\{w, l, b\}$ indicates if the matrices are defined in the domains Ω_w, Ω_l and Ω_b respectively. The global discrete linear operator are defined as

$$\boldsymbol{L}_B = \boldsymbol{M}_w - Bh_0^2 \boldsymbol{Q}_w \boldsymbol{M}_w^{-1} \boldsymbol{Q}_w, \qquad \boldsymbol{B}_d^\alpha = \tilde{\boldsymbol{Q}}_w + \alpha_{MS} h_0^2 \tilde{\boldsymbol{Q}}_w \boldsymbol{M}_w^{-1} (\boldsymbol{Q}_w \boldsymbol{M}_w^{-1} \boldsymbol{Q}_w). \tag{43}$$

Proposition 3. *The discrete variational form eq.* (42) *is well balanced: the steady hydrostatic equilibrium in eq.* (36) *with* $\bar{a} = a = 0$*, is exactly preserved.*

Proof. Identical to the continuous case in proposition 2 □

Remark 1. *The total pressure P verifies the same discrete equation in all domains. In fact, eq.* (42d) *is a consequence of the semi-discrete mass eq.* (42a) *solved in the free surface domains. In the inner domain Ω_b, the satisfaction of the mass equation $\boldsymbol{M}_b d_t + \boldsymbol{Q}_b q = 0$ is obtained by imposing it implicitly as a constrain. This provides an exact discrete consistency between the mass and pressure equations in all domains.*

3.2. Time Discretization

In this paper we implement an extrapolated backward differentiation formula of third order (eBDF3). The eBDF3 scheme has the same computational cost of the explicit Euler time integration. Thus, the eBFD3 with spectral/*hp* elements method results in a very efficient method in time and space to solve our wave-body interaction problem. Introducing the notation $f^n = f(x, t^n)$, the time derivative for eBDF3 time integration is expressed as

$$\delta f = \frac{11 f^{n+1} - 18 f^n + 9 f^{n-1} - 2 f^{n-2}}{6\delta t}, \tag{44}$$

for constant time steps δt. The nonlinear term are evaluated at time $n+1$ by a linear extrapolation. This extrapolation is

$$f^e = 3 f^n - 3 f^{n-1} + f^{n-2}. \tag{45}$$

The time step δt is chosen in relation with the mesh dimension δx through a standard CFL condition [14]. For the grid convergence studies, δt is appropriately reduced such that the error in time is always dominated by the error in space. Note that the linear operator $\boldsymbol{B}_d^{\alpha}$ is evaluated with the extrapolated depth d.

3.3. Added mass

As already mentioned, in the case of a moving body the acceleration is defined by Newton's second law

$$m_b a^{n+1} = -m_b g + \rho_w \int_{\Omega_b} \Pi^{n+1} n_z dx. \tag{46}$$

We define the vector $\boldsymbol{w}$ of the Gauss-Lobatto-Legendre integration weights giving the discrete formulation

$$m_b a^{n+1} = -m_b g + \rho_w \boldsymbol{w}^T \Pi^{n+1}. \tag{47}$$

We can prove the following proposition.

Proposition 4. *Provided that the matrix $\tilde{\boldsymbol{K}}_b$ is invertible, the discrete acceleration eq.* (47) *is*

$$(m_b + \mathcal{M}_{add})\, a^{n+1} = -m_b g - g\rho_w \boldsymbol{w}^T d_b - \rho_w \boldsymbol{w}^T \tilde{\boldsymbol{K}}_b^{-1} \left(\boldsymbol{Q}_b \boldsymbol{M}_b^{-1} \boldsymbol{Q}_b (uq)^e + \tilde{\boldsymbol{G}}_f P_f \right). \tag{48}$$

where the added mass is defined as

$$\mathcal{M}_{add} = -\rho_w \boldsymbol{w}^t \tilde{\boldsymbol{K}}_b^{-1} \boldsymbol{w}. \tag{49}$$

Moreover, in case of constant depth and flat bottom body d_b^*, it can be shown that $\tilde{\boldsymbol{Q}}_b = d_b^* \boldsymbol{Q}_b$ and the matrix $\tilde{\boldsymbol{K}}_b = d_b^* \boldsymbol{K}_b$ is positive semi-definite (PSD) and thus the added mass is non-negative

$$\mathcal{M}_{add} \geq 0. \tag{50}$$

Proof. Consider the discretized first order formulation presented in eqs. (25)- (26). For simplicity we define the free surface domain $\Omega_f = \Omega_w \cup \Omega_l$. We replace the first derivative matrix $\tilde{\boldsymbol{Q}}_b$ according to the definition in eq. (41)

$$-(\boldsymbol{D}_b + \boldsymbol{C}_{bb})\, w_b + \boldsymbol{C}_{bf} w_f = -\boldsymbol{M}_b \mathbb{1} a + \boldsymbol{Q}_b \boldsymbol{M}_b^{-1} \boldsymbol{Q}_b q u, \tag{51a}$$

$$w_b = \boldsymbol{M}_b^{-1} \left(\left(\tilde{\boldsymbol{D}}_b + \tilde{\boldsymbol{C}}_{bb} \right) P_b + \tilde{\boldsymbol{C}}_{bf} P_f \right), \tag{51b}$$

$$w_f = \boldsymbol{M}_b^{-1} \left(\left(\tilde{\boldsymbol{D}}_f + \tilde{\boldsymbol{C}}_{ff} \right) P_f + \tilde{\boldsymbol{C}}_{fb} P_b \right). \tag{51c}$$

We define the matrices $\tilde{\boldsymbol{K}}_b$ and $\tilde{\boldsymbol{G}}_f$ using the definition of w_b and w_f in eq. (51a) and collecting the matrices,

$$\tilde{\boldsymbol{K}}_b = (\boldsymbol{D}_b + \boldsymbol{C}_{bb})\, \boldsymbol{M}_b^{-1} \left(\tilde{\boldsymbol{D}}_b + \boldsymbol{C}_{bb}\right) + \tilde{\boldsymbol{C}}_{bf} \boldsymbol{M}_f^{-1} \tilde{\boldsymbol{C}}_{fb}, \tag{52a}$$

$$\tilde{\boldsymbol{G}}_f = (\boldsymbol{D}_b + \boldsymbol{C}_{bb})\, \boldsymbol{M}_b^{-1} \tilde{\boldsymbol{C}}_{bf} + \boldsymbol{C}_{bf} \boldsymbol{M}_f^{-1} \left(\tilde{\boldsymbol{D}}_f + \tilde{\boldsymbol{C}}_{ff}\right). \tag{52b}$$

From the definition of total pressure eq. (2) and inverting $\tilde{\boldsymbol{K}}_b$, we have an expression for Π

$$\Pi = \tilde{\boldsymbol{K}}_b^{-1} \boldsymbol{M}_b \mathbb{1} a - \tilde{\boldsymbol{K}}_b^{-1} \boldsymbol{Q}_b \boldsymbol{M}_b^{-1} \boldsymbol{Q}_b q u - g d_b - \tilde{\boldsymbol{K}}_b^{-1} \tilde{\boldsymbol{G}}_f P_f. \tag{53}$$

Eq. (53) is substituted in the discrete formulation of the acceleration eq. (47)

$$m_b a = -m_b g + \rho_w \boldsymbol{w}^T \left(\tilde{\boldsymbol{K}}_b^{-1} \boldsymbol{M}_b \mathbb{1} a - \tilde{\boldsymbol{K}}_b^{-1} \boldsymbol{Q}_b \boldsymbol{M}_b^{-1} \boldsymbol{Q}_b q u - g d_b - \tilde{\boldsymbol{K}}_b^{-1} \tilde{\boldsymbol{G}}_f P_f\right). \tag{54}$$

Note that $\boldsymbol{M}_b \mathbb{1} a^{n+1} = \boldsymbol{w} a^{n+1}$, in fact

$$[\boldsymbol{M}_b \mathbb{1}]_i = \int_{\Omega_b} \sum_j^{N_{dof}} \psi_i \psi_j. \tag{55}$$

From the definition of Gauss-Lobatto-Legendre basis function, we get that

$$\sum_j^{N_{dof}} \psi_j = 1. \tag{56}$$

As a consequence

$$[\boldsymbol{M}_b \mathbb{1}]_i = \left(\int_{\Omega_b} \psi_i\right), \tag{57}$$

and by analogy with the notation used for the pressure integral in eq. (47)

$$[\boldsymbol{M}_b \mathbb{1}]_i = w_i. \tag{58}$$

To show that the added mass is always non-negative for constant depth and flat bottom body, consider the quadratic function $-\boldsymbol{w}^T \boldsymbol{K}_b \boldsymbol{w} = -\boldsymbol{w}^T (\boldsymbol{D}_b + \boldsymbol{C}_{bb})\, \boldsymbol{M}_b^{-1} (\boldsymbol{D}_b + \boldsymbol{C}_{bb})\, \boldsymbol{w} + \boldsymbol{w}^T \boldsymbol{C}_{bf} \boldsymbol{M}_f^{-1} \boldsymbol{C}_{fb} \boldsymbol{w}$. The mass matrices $\boldsymbol{M}_b$ and $\boldsymbol{M}_f$ are positive definite (PD) so also their inverse [25]. From eq. (40b), we can define the matrices $\boldsymbol{D}_b + \boldsymbol{C}_{bb}$ and $(\boldsymbol{D}_b + \boldsymbol{C}_{bb})^T$

$$[\boldsymbol{D}_b + \boldsymbol{C}_{bb}]_{ij} = \int_{\Omega_b} \psi_i (\psi_j)_x dx + 0.5 \int_{\partial\Omega_b} \psi_i \psi_j \boldsymbol{n}|_{\partial\Omega_b} dx, \tag{59a}$$

$$\left[(\boldsymbol{D}_b + \boldsymbol{C}_{bb})^T\right]_{ij} = \int_{\Omega_b} \psi_j (\psi_i)_x dx + 0.5 \int_{\partial\Omega_b} \psi_i \psi_j \boldsymbol{n}|_{\partial\Omega_b} dx. \tag{59b}$$

We also know that

$$\int_{\Omega_b} (\psi_i \psi_j)_x dx = \int_{\Omega_b} (\psi_i)_x \psi_j dx + \int_{\Omega_b} \psi_i (\psi_j)_x dx = \int_{\partial\Omega_b} \psi_i \psi_j \boldsymbol{n}|_{\partial\Omega_b} dx. \tag{60}$$

Using eq. (60) in eq. (59a), it can be shown that

$$[\boldsymbol{D}_b + \boldsymbol{C}_{bb}]_{ij} = -\left[(\boldsymbol{D}_b + \boldsymbol{C}_{bb})^T\right]_{ij}. \tag{61}$$

Since the matrix $\boldsymbol{M}_b^{-1}$ is PD, it exist a unique PD matrix $\boldsymbol{B}_b$ such that $\boldsymbol{B}_b^2 = \boldsymbol{B}_b^T \boldsymbol{B}_b = \boldsymbol{M}_b^{-1}$ [25]. Thus, it holds the equivalence

$$-\boldsymbol{w}^T (\boldsymbol{D}_b + \boldsymbol{C}_{bb})\, \boldsymbol{M}_b^{-1} (\boldsymbol{D}_b + \boldsymbol{C}_{bb})\, \boldsymbol{w} = -\boldsymbol{w}^T (\boldsymbol{D}_b + \boldsymbol{C}_{bb})\, \boldsymbol{B}_b^T \boldsymbol{B}_b (\boldsymbol{D}_b + \boldsymbol{C}_{bb})\, \boldsymbol{w}, \tag{62}$$

In the same way, for the free surface-body coupling matrices

$$\left[\boldsymbol{C}_{bf}\right]_{ij} = 0.5 \int_{\partial\Omega_b \cap \partial\Omega_f} \psi_i \psi_j \boldsymbol{n}|_{\partial\Omega_b} dx, \tag{63a}$$

$$\left[\boldsymbol{C}_{fb}\right]_{ij} = 0.5 \int_{\partial\Omega_f \cap \partial\Omega_b} \psi_i \psi_j \boldsymbol{n}|_{\partial\Omega_f} dx. \tag{63b}$$

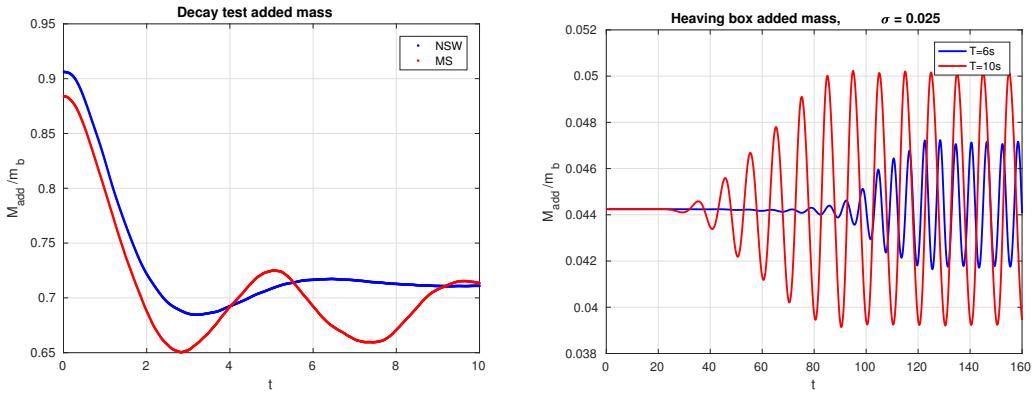

Figure 4: The added mass over the body mass in the test presented in sections 4.6 and 4.8. We see that in all cases, decay movement solved with NSW and MS in figure a and a free heaving box with different incoming waves in b, the value of the added mass is always positive

and it can be shown that

$$\left[\boldsymbol{C}_{bf}\right]_{ij} = -\left[\boldsymbol{C}_{fb}^{T}\right]_{ij}. \tag{64}$$

Since also the matrix $\boldsymbol{M}_f$ is PD, it exists a matrix $\boldsymbol{B}_f$ such that $\boldsymbol{B}_f^2 = \boldsymbol{B}_f^T\boldsymbol{B}_f = \boldsymbol{M}_f^{-1}$ and

$$-\boldsymbol{w}^T\boldsymbol{C}_{bf}\boldsymbol{M}_f^{-1}\boldsymbol{C}_{fb}\boldsymbol{w} = -\boldsymbol{w}^T\boldsymbol{C}_{bf}\boldsymbol{B}_f^T\boldsymbol{B}_f\boldsymbol{C}_{fb}\boldsymbol{w}, \tag{65}$$

As a consequence of eqs. (61) and (64), we can substitute the first $\boldsymbol{D}_b + \boldsymbol{C}_{bb}$ and $\boldsymbol{C}_{bf}$

$$\begin{aligned}
&-\boldsymbol{w}^T\left(\boldsymbol{D}_b + \boldsymbol{C}_{bb}\right)\boldsymbol{B}^T\boldsymbol{B}_b\left(\boldsymbol{D}_b + \boldsymbol{C}_{bb}\right)\boldsymbol{w} - \boldsymbol{w}^T\boldsymbol{C}_{bf}\boldsymbol{B}_f^T\boldsymbol{B}_f\boldsymbol{C}_{fb} = \\
&\quad = \boldsymbol{w}^T\left(\boldsymbol{D}_b + \boldsymbol{C}_{bb}\right)^T\boldsymbol{B}^T\boldsymbol{B}_b\left(\boldsymbol{D}_b + \boldsymbol{C}_{bb}\right)\boldsymbol{w} + \boldsymbol{w}^T\boldsymbol{C}_{fb}^T\boldsymbol{B}_f^T\boldsymbol{B}_f\boldsymbol{C}_{fb} = \\
&\quad = \left(\boldsymbol{B}\left(\boldsymbol{D}_b + \boldsymbol{C}_{bb}\right)\boldsymbol{w}\right)^T\boldsymbol{B}_b\left(\boldsymbol{D}_b + \boldsymbol{C}_{bb}\right)\boldsymbol{w} + \left(\boldsymbol{B}_f\boldsymbol{C}_{fb}\boldsymbol{w}\right)^T\boldsymbol{B}_f\boldsymbol{C}_{fb}\boldsymbol{w} = \\
&\quad = \left(\boldsymbol{B}_b\left(\boldsymbol{D}_b + \boldsymbol{C}_{bb}\right)\boldsymbol{w}\right)^2 + \left(\boldsymbol{B}_f\boldsymbol{C}_{fb}\boldsymbol{w}\right)^2 \geq 0.
\end{aligned} \tag{66}$$

So $-\boldsymbol{K}_b$ is positive semi-definite (PSD). When it is invertible also its inverse must be PSD [25] and the added mass is non-negative for constant depth. □

Remark 2. *Note that non positive added mas can occur in the free surface flow with floating structure [36]. Here, for flat structure, the above proposition shows that accounting for added mass has a stabilizing effect. This result can be generalized within an order $O(\Delta x)$ if a truncated Taylor series is introduced:*

$$\int_{\Omega_b}\varphi_i d_b(x)\partial_x\varphi_j dx \approx d_b(x_i)\int_{\Omega_b}\partial_x\varphi_j dx + C_i\|\partial_x d_b(x)\|\Delta x + O(\Delta x^2), \tag{67}$$

where C_i is a mesh dependent constant. Eq. (67) can be readily used to show that

$$\boldsymbol{Q}^T\boldsymbol{M}^{-1}\tilde{\boldsymbol{Q}} = \boldsymbol{Q}^T\boldsymbol{M}^{-1}\mathcal{D}_{d_b}\boldsymbol{Q} + O(x), \tag{68}$$

where $\mathcal{D}$ is the diagonal of $d_b(x_i)$. This leads to the conclusion that for bodies having a bounded variation profile, accounting for the added mass will still provide a stabilizing effect, at least on a fine enough grid.

For non-flat bottom body, we can not demonstrate the non-negativeness analytically. However, we have shown numerically that $\mathcal{M}_{add} \geq 0$ in figure 4. These plots show the trends of the ratio of added mass over the mass of the body in few of the tests presented in section 4. For the added mass eq. (48), we can prove the following result

Proposition 5. *The hydrostatic equilibrium eq.* (36) *is a solution of the added mass acceleration equation.*

Proof. Substitute the eq. (36) in the acceleration eq. (48)

$$0 = -m_b g - g\rho_w \boldsymbol{w}^T \bar{d}_b - \rho_w \boldsymbol{w}^T \left(\tilde{\boldsymbol{K}}_b\right)^{-1} \left(\tilde{\boldsymbol{G}}_f \bar{P}_f\right). \tag{69}$$

At the hydrostatic equilibrium, the pressure is constant through all the domains. This means that

$$\begin{aligned} \bar{d}_b \partial_x \bar{P}_b &= \tilde{\boldsymbol{Q}}_b \bar{P}_b = 0 \\ \bar{d}_f \partial_x \bar{P}_f &= \tilde{\boldsymbol{Q}}_f \bar{P}_f = 0 \end{aligned} \tag{70}$$

and the auxiliary variable $\boldsymbol{M}\bar{w}_b = \tilde{\boldsymbol{Q}}_b \bar{P}_b$ is also equal to zero. Using the matrices introduced in eq. (52)

$$\tilde{\boldsymbol{Q}}_b \bar{w}_b = \tilde{\boldsymbol{K}}_b \bar{P}_b + \tilde{\boldsymbol{G}}_f \bar{P}_f = 0 \tag{71}$$

thus $\tilde{\boldsymbol{G}}_f \bar{P}_f = -\tilde{\boldsymbol{K}}_b \bar{P}_b$. Moreover, we know by definition that $m_b = \rho_w \boldsymbol{w}^T (h_0 - \bar{d}_b)$ and eq. (69) becomes

$$0 = -\rho_w g \boldsymbol{w}^T (h_0 - \bar{d}_b) - g\rho_w \boldsymbol{w}^T \bar{d}_b + \rho_w \boldsymbol{w}^T \boldsymbol{I} \bar{P}_b. \tag{72}$$

where $\boldsymbol{I}$ is the identity matrix. Eq. (72) at equilibrium $(\bar{d}_b, \bar{P}_b)$ is satisfied. □

The strategy adopted to solve the whole problem is to evaluate at each step first the added mass $\mathcal{M}_{add}$ and the vertical acceleration of the body in eqs. (49)-(48), with the extrapolated values of the variables from the previous timestep. The updated value of the acceleration is substituted into eq. (42d), as a right hand side term, which coupled with eq. (42a) gives us $P(x, t^{n+1})$. Finally, we solve eqs. (42b) and (42c) for the updated values of the flow $q(x, t^{n+1})$. Note that all coupling conditions of the flow and elevation between outer and inner domains are accounted for by the coupling terms in the $\boldsymbol{Q}_{w,l,b}$ and $\tilde{\boldsymbol{Q}}_{w,l,b}$ matrices.

4. Numerical Results

We consider in this section different tests to demonstrate the versatility of the proposed spectral/*hp* depth-integration model given in section 3. First, we consider the wave propagation problem in hybrid modelling approach to that verify the coupled solver strategy leads to the expected convergence. Then, we consider the more complex problems with fixed, forced and free movement for a box. Finally, we seek to compare the solver with the results of CFD simulations as a validation means and to demonstrate the efficiency of the proposed numerical modelling strategy

4.1. Coupling domains with different wave models

As the coupling is enforced by flux conditions that handle only the balance of incoming and outgoing flow, we can easily couple different free surface wave models. In particular, we report here the coupling between a free surface domain with MS and one with NSW. Each domain has a length of 2π meters and is discretized over a grid of 40 elements. Two kind of waves are tested: a linear wave ($A = 10^{-6}m$, $h_0 = 0.1m$) and a nonlinear wave ($A = 0.02m$, $h_0 = 0.5m$). The simulations are presented respectively in figures 5a and 5b. The linear wave cross the different domain without alterations while the solution for the nonlinear wave shows multiple harmonics. That is due to the signal that decomposes propagating through NSW domain, as the model can not solve properly this set of waves. This test allows us to examine the behaviour of the solution at the coupled interfaces. As anticipated, the free surface elevation is continuous (the jump on the interfaces is of order 10^{-13}, close to the machine precision) and there are no oscillations at the interfaces.

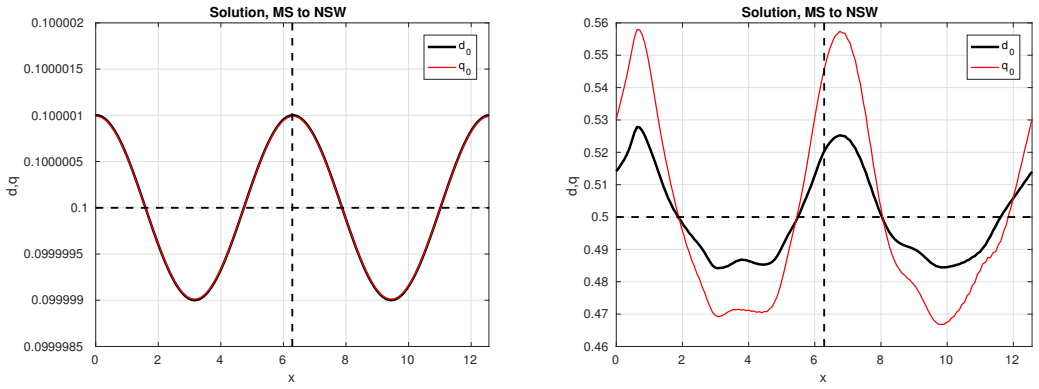

a b

Figure 5: Wave elevation at $t = 25$ s using a MS domain and a NSW domain: a linear wave case and 5b nonlinear wave case.

4.2. *Grid convergence for the free surface model*

An exact solution for the MS model does not exist. The convergence of the mixed wave model is evaluated using the manufactured solution method. We consider a known function $\zeta(x-ct) = A\cos(x-ct)$, with A the wave amplitude and c the phase speed, to be imposed as the solution of the problem, i.e.

$$\begin{aligned} P^m &= d^m(x,t) = \zeta(x-ct) + h_0, \\ u^m(x,t) &= \frac{c}{A}\zeta(x-ct), \\ q^m(x,t) &= d^m(x,t)u^m(x,t) = \frac{c}{A}\zeta(x-ct)(\zeta(x-ct)+h_0). \end{aligned} \tag{73}$$

Equation (73) will not exactly satisfy the original differential equation and the substitution will result in a residual $r(\zeta) \neq 0$. This residual is treated has the source term for the differential equations considered, such that for NSW and MS free surface models, we have

$$\begin{aligned} &d_t + q_x = r_d(\zeta), \\ &q_t + (uq)_x + gd(P)_x = r_q^{(NSW)}(\zeta), \\ &q_t + (uq)_x + gd(P)_x - \left(\tfrac{1}{3} + \alpha_{MS}\right)h_0^2 q_{xxt} - \alpha_{MS}h_0^3 d_{xxx} = r_q^{(MS)}(\zeta). \end{aligned} \tag{74}$$

Now the function $\zeta(x-ct)$ is the exact solution of the problem and that can be compared to the numerical one for a convergence study. We have chosen $\zeta(x-ct) = A\sin(x-ct)$ since it is a simple, periodic, $C^\infty(\mathbb{R}\times\mathbb{R}_+)$ function of which we can calculate all the derivatives. Thus the residuals $r(\zeta)$ are known exactly.

This residual terms act as source terms for the equation and are discretized in space. The discretized model is

$$\boldsymbol{A}\boldsymbol{U}_t = \boldsymbol{RHS} + \boldsymbol{M}\bar{r}. \tag{75}$$

The source term is evaluated exactly at time step t_{n+1}. The convergence of the NSW and MS equations is shown in figure 6 $N_{el} = [6, 12, 24]$ and $p = [1, 2, 3, 4, 5]$. As seen in figure 6, we reach the optimal rate of convergence $p+1$ for odd polynomial order and sub-optimal rate p for even polynomial order. The sub-optimal convergence rate is caused by the choice of centred fluxes [8].

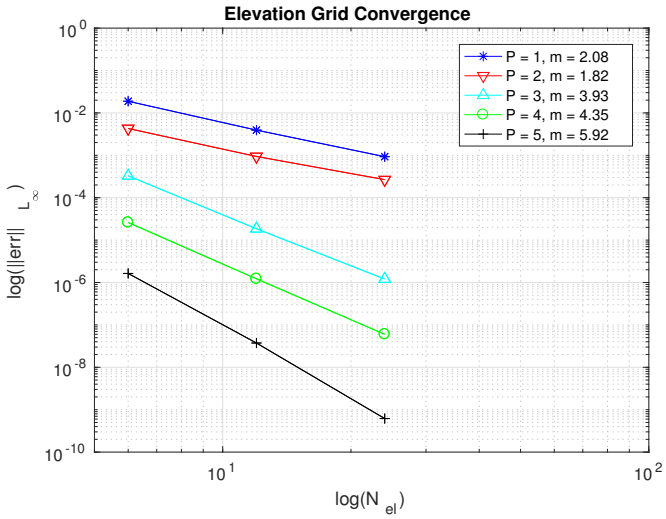

Figure 6: Convergence trend in a MS-NSW-MS model, with number of elements $N_{el} = [6, 12, 24]$ and polynomial orders $p = [1, 2, 3, 4, 5]$.

4.3. Grid convergence for a fixed inner model

We use a similar approach to test the convergence for a manufactured model with a fixed structure in the central domain, see figure 7. The manufactured solution considered reads

$$\begin{aligned} P^m_{tot} &= g(\zeta(x-ct)+h_0), \\ q^m(x,t) &= \frac{c}{A}\zeta(x-ct)(\zeta(x-ct)+h_0), \\ d^m(x,t) &= \begin{cases} \zeta(x-ct)+h_0\,, & x \in \Omega_w, \\ h_0 - h_d\,, & x \in \Omega_b. \end{cases} \end{aligned} \tag{76}$$

where h_d is the draft of the body. As for the free surface convergence test, the models solved are MS for the free surface domains and NSW in the body domain. The convergence of the method is presented in figure 8 for the depth and total pressure. This can be due to the discontinuity in depth and nonlinear term which can not be solved exactly and results in oscillation around the coupling nodes.

We remark here on the efficiency of the spectral element method: considering a simulation of one period $T = 1.95s$, we use $N_t = 5000$ time steps and we test different meshes. The efficiency of the model has been checked for the medium size mesh, with $N_{el} = 12$ for each domain. The error drops with five orders of magnitude going from $p = 1$ to $p = 5$ while the computational time remains comparable. On the other hand, if we want to reach a similar precision with linear elements, we need a much finer grid with 1500 DOF per domain against the 60 DOF of the high polynomial order and the computational time grows with 5 orders of magnitude.

4.4. Time convergence

The time convergence of the method is evaluated using the manufactured solution presented in figure 7 with $N_{el} = 12$ elements per domain and polynomial order $p = 5$. Normally, to maintain stability of the solution for the eBDF3, the timestep δt is taken to be always small than the space element dimension δx determined by a CFL condition [14], as we presented in section 3.2. Thus, comparing the numerical solution to the exact one, the space error will always dominate on the time one. We have evaluated a reference numerical solution with a small time step (number of time step $N_t = 64000$ over two wave periods) and the convergence is computed using this solution. The resulting convergence plot is reported in figure 9. The rate of convergence in time is seen to be 3, same as the theoretical convergence rate of the eBDF3 scheme.

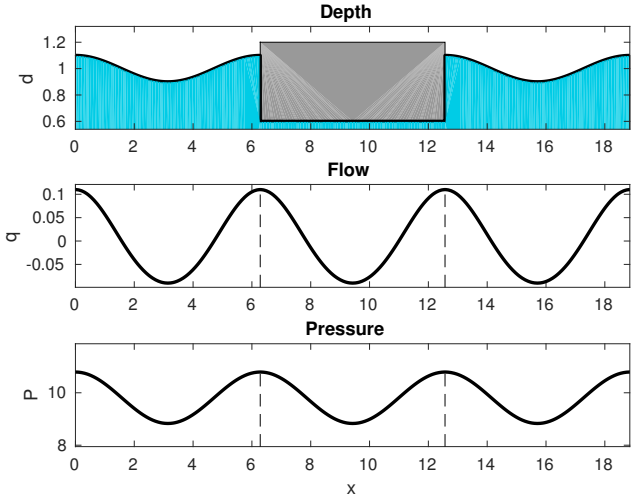

Figure 7: Solution of the manufactured problem for $p = 5$, with number of elements $N = 12$, final time $T = 2s$.

4.5. Forced motion test

This test includes forced oscillation of a box with a round bottom [29], shown in figure 10a. The body is placed with its center at $x = 0$ and the water flume extends for $200m$ before and after it. The body is composed by a rectangular box of height $H = 2R\sin(\pi/3) - R$ and width $2R$ The circular segment has radius $2R$ with the center placed on the vertical line passing through the middle point. The density of the object is half the density of water, $\rho_b = 0.5\rho_w$. We can easily evaluate the mass of the object as $m = \rho_b \mathcal{V}$ where $\mathcal{V}$ is the volume

$$\mathcal{V} = R^2\left(\sqrt{3} - 2 + \frac{2\pi}{3}\right). \tag{77}$$

In the test we use $R = 10m$. The fluid domain is defined with a still-water depth $h_0 = 15m$ and density of water $\rho_w = 1000kgm^{-3}$. The structure moves in a forced motion starting from initial position $z_{C,eq} = 4.57m$ and an oscillation of $2m$ over $10s$ time. The height $z_{C,eq}$ corresponds to the equilibrium in case of the free floating body and can be calculated as

$$z_{C,eq} = \frac{R}{2}\left(1 - \frac{\rho_b}{\rho_w}\right)\left(\sqrt{3} - 2 + \frac{2\pi}{3}\right). \tag{78}$$

The numerical setting is: polynomial order $p = 3$, $N_w = 25$ free surface elements and $N_b = 5$ internal elements.

In the hydrostatic case, we have an analytic solution for the water elevation at the contact points x_+ and x_-, where water and body interact, [29]. The evolution of the water level at $x_\pm$ is described by

$$d_e(t, x_\pm) = \left(\tau_0\left(\frac{x_+ - x_-}{4\sqrt{g}} v_g\right)\right)^2, \tag{79}$$

$v_G = d_t$ is the given velocity of the center of gravity of the object. The parameter τ_0 is obtained from

$$\tau_0(r) = \frac{1}{3}\left(\sqrt{h_0} + C(r) + \frac{h_0}{C(r)}\right), \tag{80}$$

with $C(r)$ given by

$$C(r) = \frac{3}{2}\left(-4r + r_0 + \sqrt{r(r - r0)}\right)^{\frac{1}{3}}, \tag{81}$$

and $r_0 = \frac{4}{27}h_0^{\frac{3}{2}}$.

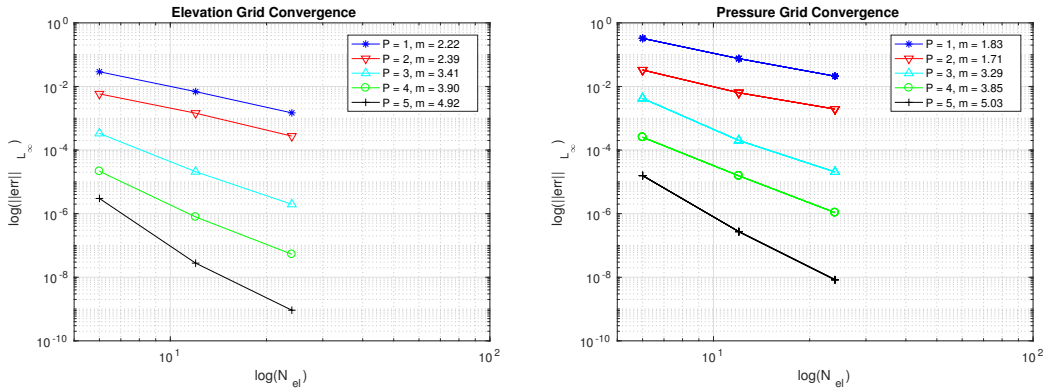

Figure 8: Convergence trend in a MS-NSW-MS model, in figure a for the depth variables and in figure b for the total pressure variable.

Figure 10c shows the position of the contact point in time. The numerical solution presents the same behaviour of the exact solution. The error on the mass is evaluated with the body at the equilibrium position: the method conserves the mass within the limits of the finite domain and the absorption layer at the boundary. The figure 11 presents a convergence study. We get a lower rate of convergence for all the mesh tested, compared to the results of sections 4.2 and 4.3. This is probably due to the fact that the initialization of the first two steps of eBDF3 method are evaluated with Euler and the error is then propagated to the rest of the simulation.

4.6. Decay test

For the decay test, we consider the same structure as in the previous test freely floating in the vertical direction. The body is released from an initial position $z_{C,0}$ different from the equilibrium position $z_{C,eq}$. In the simulation the body starts with the center of gravity below the water line $z_{C,0} = z_{C,eq} - 2m$ and it returns to the equilibrium position. We can validate the model solving the semi-analytical solution for the movement of the body's center of gravity, given by the differential equation [29]

$$\begin{cases} (m_b + m_{add})\ddot{\delta_G} = -c\delta_G - \nu(\dot{\delta_G}) + \beta(\delta_G)(\dot{\delta_G})^2 \\ (\delta_G, \dot{\delta_G})(t=0) = (\delta_G^0, 0), \end{cases} \tag{82}$$

the parameters $\nu(\dot{\delta_G})$ and $\beta(\delta_G)$ are defined as

$$\begin{aligned} \nu(\dot{\delta_G}) &= \rho_w g(x_+ - x_-)\left[h_0 - \left(\tau_0\left(\frac{x_+ - x_-}{4\sqrt{g}}\dot{\delta_G}\right)\right)^2\right], \\ \beta(\delta_G) &= \rho_w \int_{x_-}^{x_+} \frac{x - x_0}{h_w}\partial_x\left(\frac{(x-x_0)^2}{h_w}\right)dx, \end{aligned} \tag{83}$$

with $h_w(t) = d_{eq} + \delta_G(t)$ the position of the wetted surface, d_{eq} the geometry of the bottom of the body at rest and $\zeta_{e,\pm} = \zeta_e(t, x_\pm) = d_e(t, x_\pm) - h_0$. The added mass term m_{add} and the stiffness coefficient c

$$\begin{aligned} &m_{add} = \rho_w Var(x)\alpha \quad \alpha = \int_{x_-}^{x_+} \frac{1}{h_w}dx, \\ &c = \rho_w g(x_+ - x_-). \end{aligned} \tag{84}$$

We define a variance operator as

$$\begin{aligned} &Var(f) = \langle f^2\rangle - \langle f\rangle^2, \\ &\langle f\rangle = \frac{1}{\int_{x_-}^{x_+}\frac{1}{h_w}}\int_{x_-}^{x_+}\frac{f}{h_w}dx. \end{aligned} \tag{85}$$

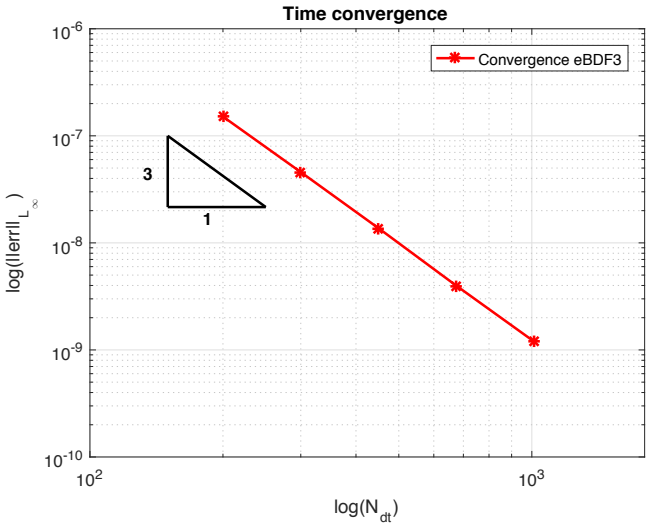

Figure 9: Time Convergence for the fixed manufactured test

The ODE eq. (82) is solved with a eBDF3 time integration scheme, such that the integration is consistent with one of the numerical problem. In figure 12c we see the tracking of the center of gravity and the semi-analytical solution and the numerical solution give comparable results. As in the previous test the total mass is conserved in the limit of the boundary wave absorption.

4.7. Fixed pontoon

The case considers a weakly nonlinear solitary wave propagating past a rectangular box [16, 31, 43]. In particular, we are going to concentrate reproducing the VOF-RANS results in [31] and FNPF results [16]. We consider a pontoon of length $L = 5m$ and draft $T_0 = 0.4m$ in a flume of constant still water depth $h_0 = 1.0m$. The total length of the flume is $185m$ of which $90m$ before the body and $90m$ after. The two wave gauges are located at $G_1 = -31.5m$ and $G_2 = 26.5m$ assuming the center of the box located at $x_c = 0m$ as shown in figure 13. The incoming solitary wave is defined by the equation from [4] and has a non-dimensional amplitude $\frac{A}{h_0} = 0.1$. The simulation is done with a mesh of $N_w = 25$ elements on the free surface domain and $N_b = 5$ elements for the body to have a better resolution, with a polynomial order $p = 3$.

We can not use the NSW model since the solitary wave is dispersive and it will not be able to solve it correctly, subsequently the MS model must be used in the outer domain. Anyway, because of proposition 1, we solve the NSW equations in the inner domain. Since the coupling between MS and NSW has been proven effective, especially for free surface flow, we set a small free surface layer around the pontoon where NSW is solved. This layer length must be calibrated and for the purpose of the fixed pontoon we kept it as small as possible to avoid the loss of the dispersive characteristic of the reflected and transmitted waves. Figure 14 shows the solution at two different times. The problem is solved correctly, with the wave transmitting and reflecting smoothly against the structure. The comparison between the elevation registered by the gauges in the VOF-RANS simulation and the MS is presented in figure 15a. The wave generated is not perfectly coincident with the wave of the original study, due to the fact that we do not have any information but the wave elevation. This results shows little discrepancies between our solution and the VOF-RANS one, in particular the elevation of the transmitted wave is over-predicted and the first peak of the trail of the reflected wave is under-predicted. Regardless, the simpler Boussinesq model can still capture the salient characteristics of the transmitted and reflected waves. The figure 15b shows the total water mass during the simulation, the drops from time $t = 0s$ to $t \approx 20s$ and at the final time, represent the absorption of a trail from the incident soliton wave and of the resulting waves in the sponge zone. Anyway we can see that, once the trail is absorbed (around $t \approx 20s$) and before time $t \approx 37s$ when the waves are absorbed, the mass is conserved.

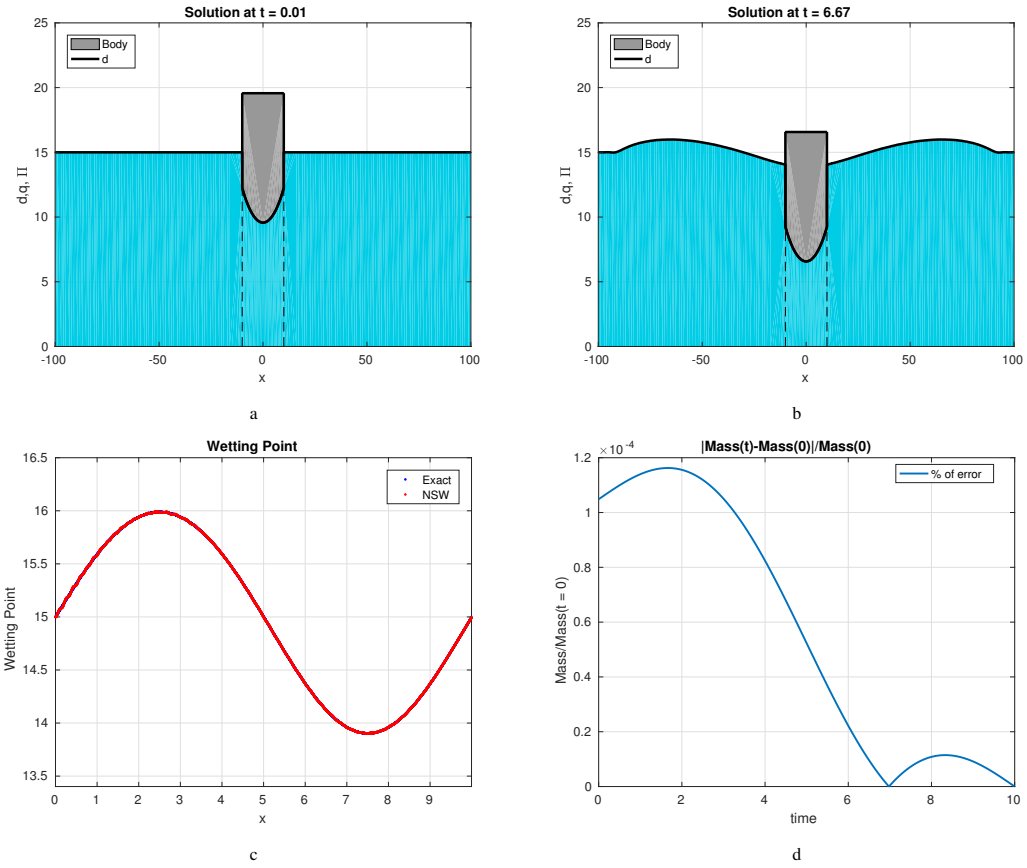

Figure 10: Snapshot of the forced motion test case: a initial state, , b solution at $t = 6.66s$. Figure c shows the evolution of the contact point and the exact solution from eq. (79). Figure d shows the amount of error on the total mass during the simulation.

4.8. Heaving body

We consider a heaving box interacting with a stream function wave [18]. The body is a rectangular box of length $l = 6m$ and height $= 10m$, with a displacement volume of $30m^2$. Because of the characteristics of the waves generated, the outer domain must be solved with the MS equations. As in section 4.7 we define a small free surface layer around the body where we solve the NSW equations, coupled with the inner NSW model. The layer here is calibrated to be long enough such that we avoid the propagation of dispersive terms under the body, where they are equal to zero and short enough to permit the propagation of the wave with minimal distortions. In practice, we have seen that $L_{NSW} = \frac{\lambda}{5}$, gives acceptable results.

We tested three set of waves of increasing steepness $\sigma = \frac{A}{\lambda}$, where A is the wave amplitude and λ the wave length. These are listed in the table 1. The main results in figure 17 are presented in terms of the Response Amplitude Operator (RAO), which is evaluated as

$$RAO = \frac{\max(\eta_i) - \min(\eta_i)}{2A}, \tag{86}$$

where η_i is the elevation of the body. We notice that, for linear waves in figure 17a, we can retrace the behavior of the linear model, with the characteristic peak at the resonance frequency. For wave with a low steepness of $\sigma = 0.025$, we have a RAO close to the CFD model where the peak at $T = 6s$ is about half the respons of the linear model. For larger wave steepness the RAO, in figure 17c, of the Boussinesq model has a value halfway between the linear and the RANS result. Note that for the fastest and shortest waves ($T < 6s$) we do not have any result for the Boussinesq

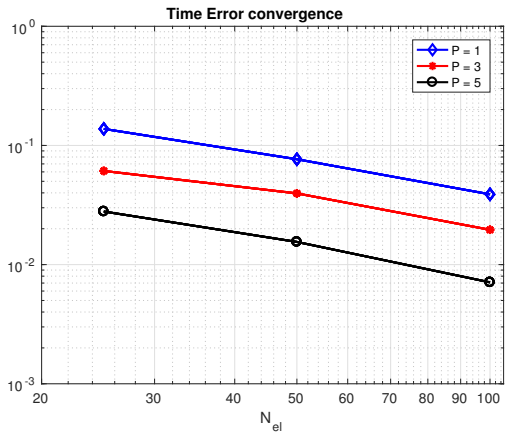

Figure 11: Convergence in time for the forced motion test

Table 1: Period, amplitude and steepness of the wave tested

Period $T[s]$	Amplitude $A[m]$	Steepness $\sigma[-]$
6.00	2.75×10^{-3}	10^{-4}
7.00	3.6×10^{-3}	10^{-4}
8.01	4.45×10^{-3}	10^{-4}
9.99	6.05×10^{-3}	10^{-4}
5.99	0.69	0.025
6.99	0.9	0.0249
8.01	1.12	0.025
10.01	1.53	0.025
5.97	1.38	0.0495
6.95	1.8	0.0494
7.92	2.23	0.0497

model as we are outside its application window, suggesting that a Boussinesq model with improved properties should be used instead.

The performance of the RANS and the Boussinesq models are presented in table 2 in the form of computational time per wave period. The RANS simulations use existing codes on OpenFOAM [39] with a mesh of 250 000 cells for the waves of period $T = 6s$ and of 350 000 cells in the other cases. The Boussinesq simulations are done on a in-house code in Matlab [35] with a mesh of 51 elements in total and of polynomial order $p = 3$. As we can see from the table 2, the computational time per period used by the Boussinesq model is two to three orders of magnitude smaller than the CFD ones. This, together with the numerical results presented in figure 17, confirm that the Boussinesq model is a cost effective alternative to a full RANS model if applied within the range of validity.

Table 2: Computational effort per wave period for the CDF and Boussinesq models

σ	Period $T[s]$	CFD $[s/T]$	Boussinesq $[s/T]$
0.025	5.99	52 000	92
	6.99	77 000	123
	8.01	92 000	143
0.05	5.97	71 000	102
	6.95	120 000	120
	7.92	150 000	145

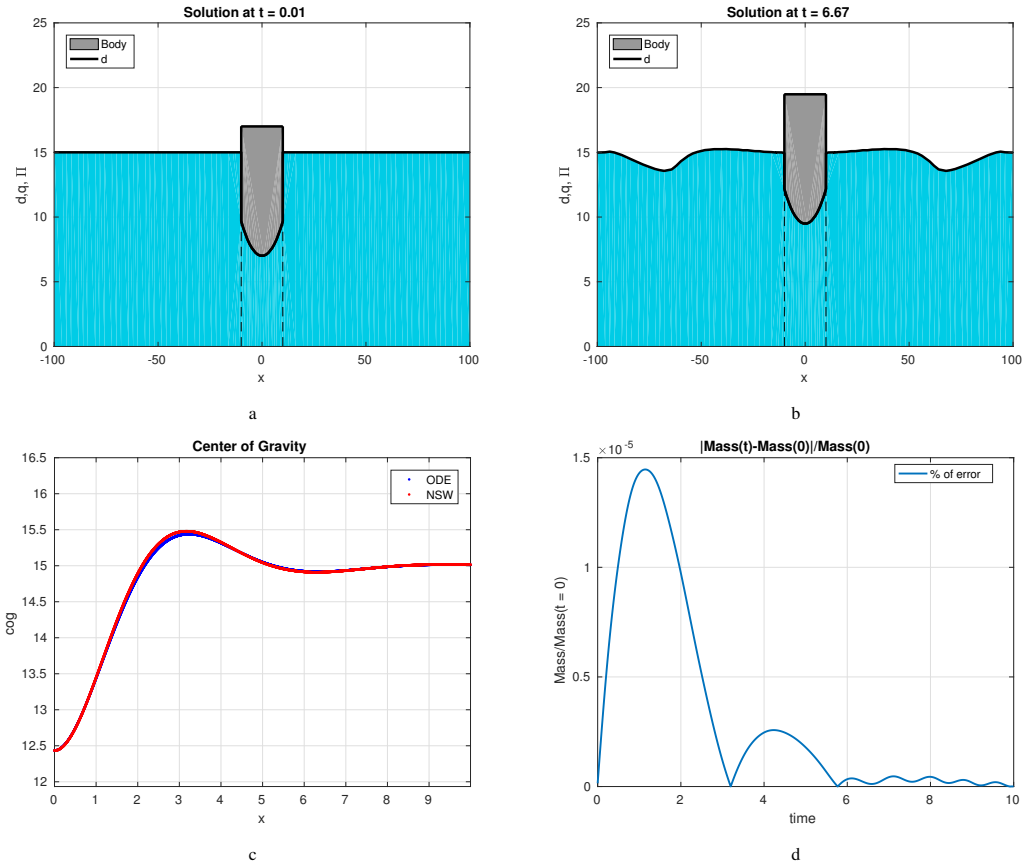

Figure 12: Snapshot of the decay test case: a initial state, 12b solution at $t = 6.66s$. Figure c shows the evolution of the center of gravity and the exact solution and figure d the conserved mass of water during the simulation.

4.9. Multiple bodies

With our framework, we can use the domain decomposition to simulate multiple bodies. In this section we consider a two bodies configuration, as shown in figure 18. Each body can be alternatively fixed or a heaving. Both bodies have length $l = 6m$ and height $h_b = 10m$. The dimension of the free surface domains is defined by the length of the wave tested, such that we can accommodate the generation and the absorption layer. The left free surface domain is 5λ long, the central domain is 2λ and the last domain is 4λ. The NSW layer around the bodies is a single element of length equal to a fifth of a wave length. The polynomial order is $p = 3$.

The figure 19 shows the response of the moving bodies of the simulations to four set of waves of period $T = [6, 7, 8, 10]s$ and steepness $\sigma = [0.0001, 0.025]$. We can see from the figure 19, that the interaction of the transmitted and reflected waves for the two bodies affects the RAO. We can see that, a part from the short linear wave where the single body (the dashed line in the plots) is at resonance frequency, the first body (blue stars and squares $*$, $\square$) benefits by the reflected waves on the second one (red Xs and triangles $\times$, $\triangleleft$), especially when the latter is another heaving body. It is interesting to notice that the variations of the RAO of the two bodies present similar trends to the single body RAO. This is probably do to the fact that the space between the to bodies is not fixed through the different simulations but it is always proportional to the wave length. We expect that the RAO can vary with less predictable trends in case the distance is fixed. This can be seen for example in figure 20, where the distance between the two bodies is fixed at 20 meters. In this case the reflected wave has a dampening impact on the movement of the first body, resulting in it having a smaller movement than the second one in most cases. This test shows also the importance, in the future, to be able to optimize the placement of several bodies in such a way that the constructive behaviors are

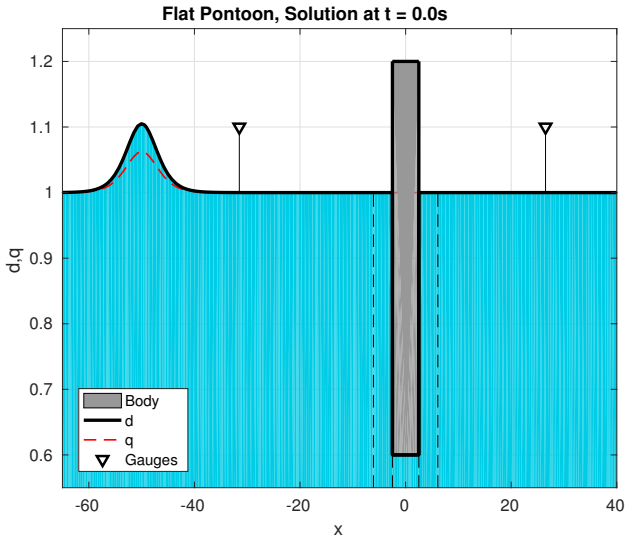

Figure 13: Set of the fixed pontoon problem.

enhanced and the destructive ones minimized.

5. Conclusion

We have presented a nonlinear numerical model for wave-body interaction using Madsen and Sørensen equations. These models are based on depth-integrated Boussinesq-type equations, a computationally efficient method for wave propagation in near-shore waters. The unified approach of Jiang [26] has inspired the model, as has the recent work of Lannes [29]. The model uses continuous spectral/hp element discretization in the different domains and are coupled by numerical fluxes [21]

We tested the model using manufactured solutions and showed the exponential convergence. In addition, we have validated our model against analytical solutions as well as CFD simulations. With the nonlinear shallow water model, we can reproduce the results of Lannes [29] and we have agreement with the exact and semi-analytical solutions. These results show that we can simulate different shapes of body. The simulation of the Madsen and Sørensen model for the fixed pontoon shows a similar outcomes for our Boussinesq model and the CFD solution by Lin [31]. The heaving floating body simulations show agreement with assessed result for linear and small steepness wave and a clear improvement in case of medium steepness compared to the linear model. Moreover, the computational time of the Boussinesq model is few order of magnitude smaller than the RANS model, making it an efficient tool for the simulation of wave-body interaction. The next step is to include some form of optimal control such that we can optimize the power output of the device. However, there are minor problems mainly related to instabilities that arise in the MS-NSW coupling or in evaluation the inner pressure. A smoothing and stabilizing method should be implemented for the pressure.

In spite of these challenges ahead we believe the present work indicates that a medium-fidelity unified Boussinesq based model can bring benefits in terms of efficiency without compromising on the accuracy of the results, if applied within the application window of the underlying Boussinesq equation. In ongoing work, we will consider the extension to two horizontal spatial dimensions as well as allowing the body to move in more degrees of freedom.

Acknowledgement

This work was performed within the Ocean ERANET project MIDWEST, funded by the French agency ADEME, Swedish Energy Agency SWEA and Portuguese agency FCT. We warmly thank Dr. D. Lannes for many useful and

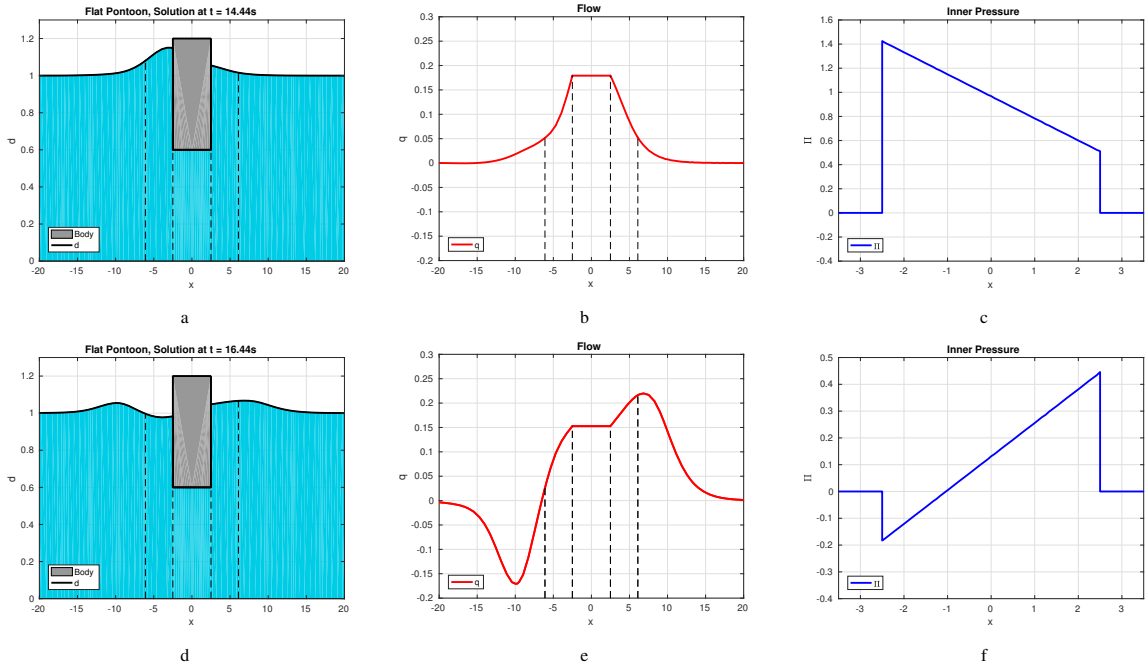

Figure 14: Snapshot of the pontoon interacting with the incoming soliton at maximum and minimum wave elevation ($time = [14.44, 16.44]s$): a and d wave elevation, b e wave flow and c and f Inner pressure.

interesting discussions and suggestions.

References

[1] Abbott, M.B., Petersen H.M. and Skovgaard O. Computations of short waves in shallow water. Coastal Engineering (1978): 414-433.

[2] Abbott, M.B., Petersen H.M. and Skovgaard O. On the numerical modelling of short waves in shallow water. Journal of Hydraulic Research 16.3 (1978): 173-204.

[3] Agamloh, E. B., Wallace, A. K. and von Jouanne, A. Application of fluid–structure interaction simulation of an ocean wave energy extraction device. Renewable Energy 33.4 (2008): 748-757.

[4] Bonneton, P., Chazel F., Lannes D., Marche F. and Tissier M. A splitting approach for the fully nonlinear and weakly dispersive Green–Naghdi model. Journal of Computational Physics 230.4 (2011): 1479-1498.

[5] Brocchini M. A reasoned overview on Boussinesq-type models: the interplay between physics, mathematics and numerics. Proc. R. Soc. A. 469.2160 (2013): 20130496.

[6] Castro M.J., LeFloch P.G., Muñoz-Ruiz M.L., Parés C.. Why many theories of shock waves are necessary: Convergence error in formally path-consistent schemes. Journal of Computational Physics 227.17 (2008): 8107-29.

[7] Chen, X.N. and Sharma, S. A slender ship moving at near-critical speed in a shallow channel. Journal of Fluid Mechanics 291 (1995): 263-285.

[8] Cockburn, B. and Shu, C.-W. The local discontinuous Galerkin method for time-dependent convection-diffusion systems. SIAM Journal on Numerical Analysis, 35.6 (1998): 2440-2463.

[9] Cummins, W. E. The impulse response function and ship motions. No. DTMB-1661. David Taylor Model Basin Washington DC, (1962).

[10] Dumbser M., Castro M., Parés C., Toro E.F. ADER schemes on unstructured meshes for nonconservative hyperbolic systems: Applications to geophysical flows. Computers & Fluids 38.9 (2009): 1731-48.

[11] Dumbser, M. and Facchini, M. A space-time discontinuous Galerkin method for Boussinesq-type equations. Applied Mathematics and Computation 272 (2016): 336-346

[12] Duran, A., Dutykh D. and Mitsotakis D. On the Galilean invariance of some nonlinear dispersive wave equations. Studies in Applied Mathematics 131.4 (2013): 359-388.

[13] Duran, A. and Marche, F. Discontinous-Galerkin discretization of a new class of Green-Nagdhi equations. Communications in Computational Physics 17.3 (2015):572-588.

[14] Engsig-Karup A.P., Eskilsson C., Bigoni D. A stabilised nodal spectral element method for fully nonlinear water waves. Journal of Computational Physics 318 (2016):1-21.

[15] Engsig-Karup, A.P., Hesthavem J.S., Bingham, H. and Madsen. P. Nodal DG-FEM solutions of high-order Boussinesq-type equations. Journal of Engineering Mathematics 56 (2006):351-370.

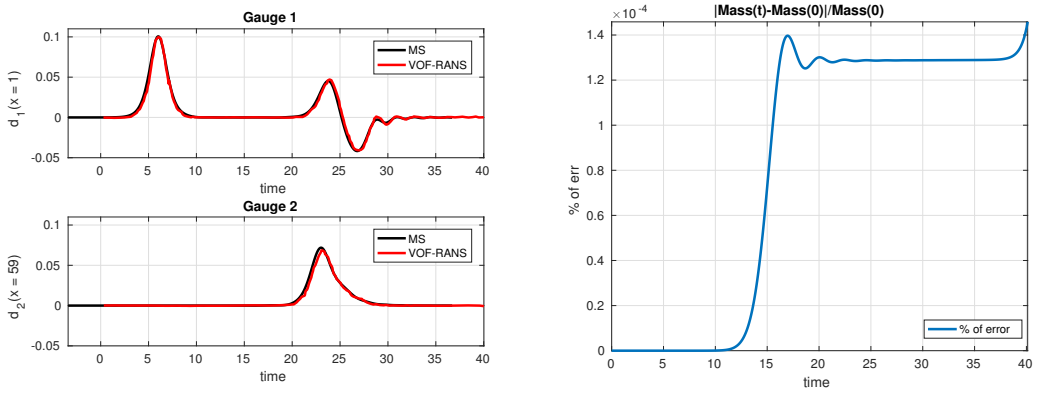

a b

Figure 15: a Elevation at the two gauges; b, error in the total water mass during the simulation.

[16] Engsig-Karup, A.P., Monteserin C. and Eskilsson C. A Stabilised Nodal Spectral Element Method for Fully Nonlinear Water Waves, Part 2: Wave-body interaction. arXiv preprint arXiv:1703.09697 (2017).

[17] Ertekin, R., Webster, W. and Wehausen, J. Waves caused by a moving disturbance in a shallow channel of finite width. Journal of Fluid Mechanics 169 (1986): 275-292.

[18] Eskilsson, C., Palm, J., Engsig-Karup, A.P., Bosi, U. and Ricchiuto, M. Wave Induced Motions of Point-Absorbers: a Hierarchical Investigation of Hydrodynamic Models. 11th European Wave and Tidal Energy Conference (EWTEC). (2015).

[19] Eskilsson, C., Palm J., Kofoed J. P. and Friis-Madsen E. CFD study of the overtopping discharge of the Wave Dragon wave energy converter. Renewable Energies Offshore (2015): 287-294.

[20] Eskilsson, C. and Sherwin S.J. A discontinuous spectral element model for Boussinesq-type equations, Journal of Scientific Computing 17.1 (2002): 143-152.

[21] Eskilsson, C. and Sherwin S.J. Spectral/hp discontinuous Galerkin methods for modelling 2D Boussinesq equations, Journal of Computational Physics 212.2 (2006): 566-589.

[22] Filippini, A.G, Bellec S., Colin M. and Ricchiuto M. On the nonlinear behaviour of Boussinesq type models: Amplitude-velocity vs amplitude-flux forms, Coastal Engineering 99 (2015): 109-123 .

[23] Godlewski E., Parisot M., Sainte-Marie J. and Wahl F. Congested shallow water model: roof modellling in free surface flow, ESAIM:M2AN (2018)

[24] Hesthaven JS, Warburton T. Nodal discontinuous Galerkin methods: algorithms, analysis, and applications. Springer Science & Business Media (2007).

[25] Horn RA, Johnson CR. Matrix analysis. Cambridge university press; (1990).

[26] Jiang, T. Ship waves in shallow water. Fortschritt-Berichte VDI Reihe 12, Verkehrstechnik, Fahrzeugtechnik; (2001).

[27] John, F. On the motion of floating bodies. Part I. Communications on Pure and Applied Mathematics 2 (1949):13-57

[28] Karniadakis, G. and Sherwin S.J. Spectral/hp element methods for computational fluid dynamics, Oxford University Press (2013).

[29] Lannes, D. On the dynamics of floating structures, Annals of PDE 3.1 (2017): 11.

[30] Lannes, D., private communications and notes.

[31] Lin, P. A multiple-layer σ-coordinate model for simulation of wave–structure interaction. Computers & fluids 35.2 (2006): 147-167.

[32] Madsen, P.A. and Schäffer H.A. A review of Boussinesq-type equations for surface gravity waves. Advances in Coastal and Ocean Engineering (1999): 1-94.

[33] Madsen, P.A. and Sørensen O.R. A new form of the Boussinesq equations with improved linear dispersion characteristics. Part 2. A slowly-varying bathymetry. Coastal Engineering 18.3-4 (1992): 183-204.

[34] Martinelli, L. and Ruol P. 2D Model of floating breakwater dynamics under linear and nonlinear waves. COMSOL users conference. (2006).

[35] MATLAB and Statistics Toolbox Release 2016b, The MathWorks, Inc., Natick, Massachusetts, United States.

[36] McIver M. and McIver P. The added mass for two-dimensional floating structures. Wave Motion, 64, pp.1-12. (2016)

[37] Muñoz-Ruiz, M.L. and Parés, C. On the convergence and well-balanced property of path-conservative numerical schemes for systems of balance laws. Journal of Scientific Computing 48.1-3 (2011): 274-295.

[38] Nørgaard, J. and Andersen, T. Investigation of wave transmission from a floating Wave Dragon wave energy converter. In Proceedings of the 22nd International Offhore and Polar Engineering Conference, Rhodes, Greece (2012)

[39] OpenCFD Ltd (2014). OpenFOAM homepage. [Online]. OpenCFD Ltd. Available http://www.openfoam.org.

[40] Palm, J., Eskilsson, C., Paredes, G. M. and Bergdahl, L. CFD simulation of a moored floating wave energy converter. In Proceedings of the 10th European Wave and Tidal Energy Conference, Aalborg, Denmark (Vol. 25). (2013)

[41] Peregrine, D.H. Long waves on a beach. Journal of fluid mechanics 27.4 (1967): 815-827.

[42] Ricchiuto, M. and Filippini, A. G. Upwind residual discretization of enhanced Boussinesq equations for wave propagation over complex bathymetries. Journal of Computational Physics 271 (2014): 306-341.

[43] Rijnsdorp, D.P. and Zijlema M. Simulating waves and their interactions with a restrained ship using a non-hydrostatic wave-flow model.

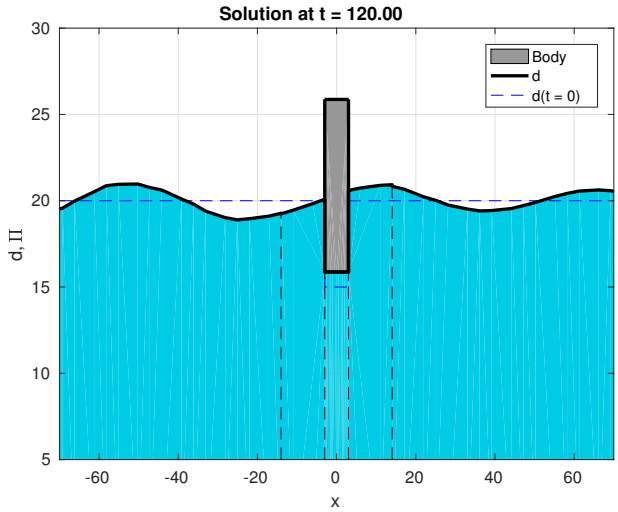

Figure 16: Particular of the heaving body after $120s$, for a stream wave of period $T = 6s$ and steepness $\sigma = 0.025$.

Coastal Engineering 114 (2016): 119-136.

[44] Samii, A. and Dawson, C. An explicit hybridized discontinuous Galerkin method for Serre-Green-Nagdhi wave model. Computer Methods in Applied Mechanics and Engineering 330 (2018): 447-470.

[45] Toro, E.F. Riemann solvers and numerical methods for fluid dynamics: a practical introduction. Springer Science & Business Media. (2013).

[46] Yan, J. and Shu, C.-W. Local discontinuous Galerkin methods for partial differential equations with higher order derivatives. Journal of Scientific Computing, 17.1-4 (2002): 27-47.

[47] Yu, Y.H. and Ye, L. Reynolds-Averaged Navier Stokes simulation of the heave performance of a two-body floating-point absorber wave energy system. Computers & Fluids 73 (2013): 104-114.

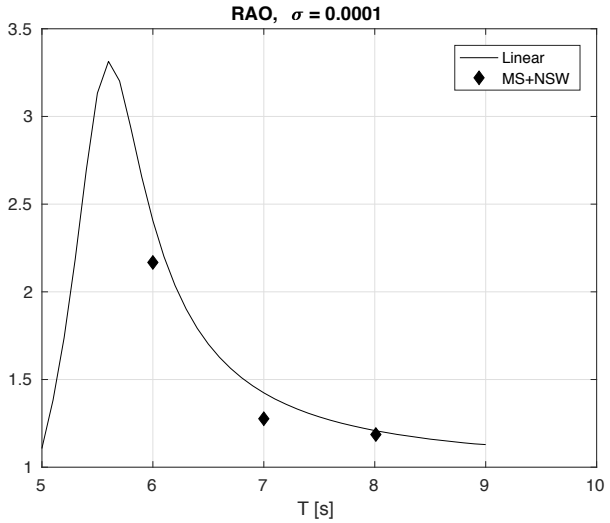

a

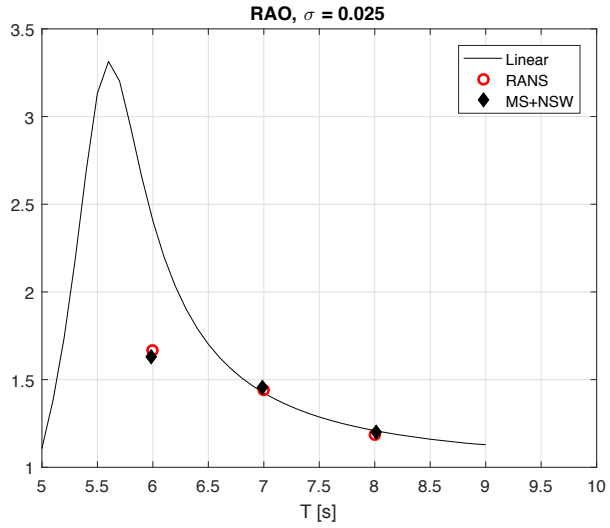

b

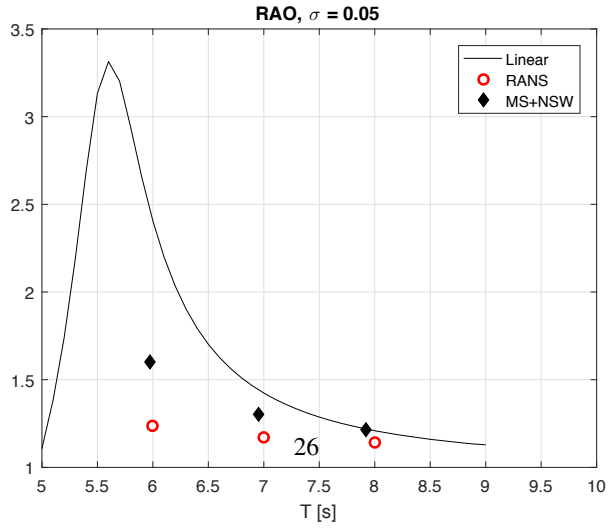

c

Figure 17: RAO plot for a linear wave of steepness $\sigma = 0.0001$ in figure a, for a stream wave of steepness $\sigma = 0.025$ in figure b and for a stream wave of steepness $\sigma = 0.05$ in figure c.

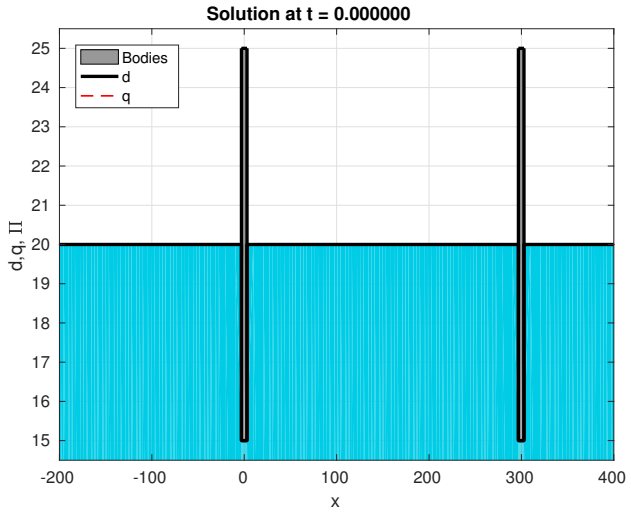

a

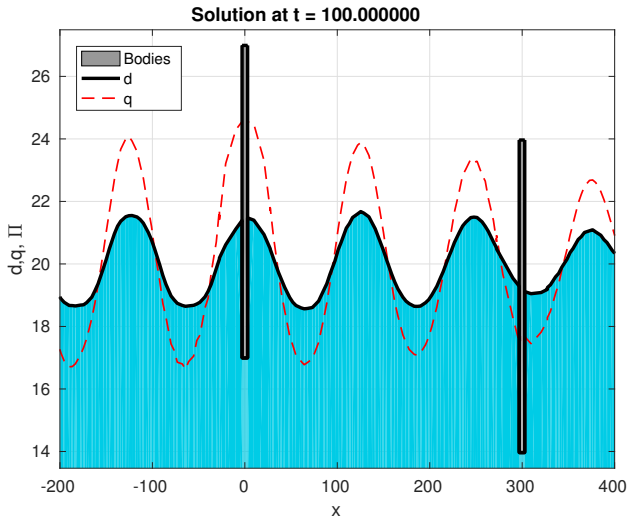

b

Figure 18: Multi body problem. Each body can be either a fixed pontoon or a heaving body. In figure a the initial set up and in figure b the simulation of two heaving bodies with a wave of period $T = 10s$ and steepness $\sigma = 0.025$

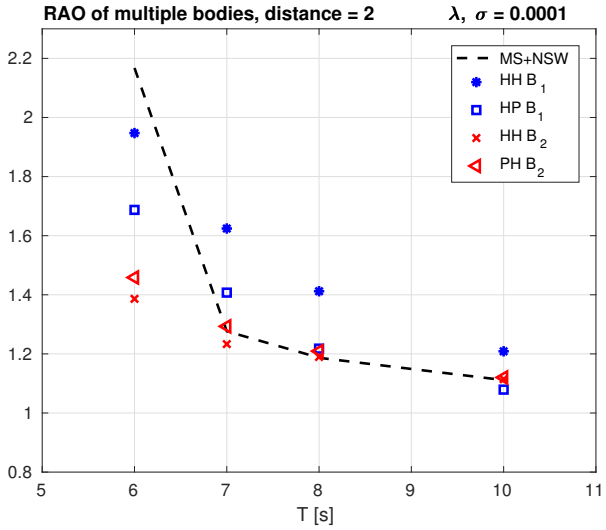

a

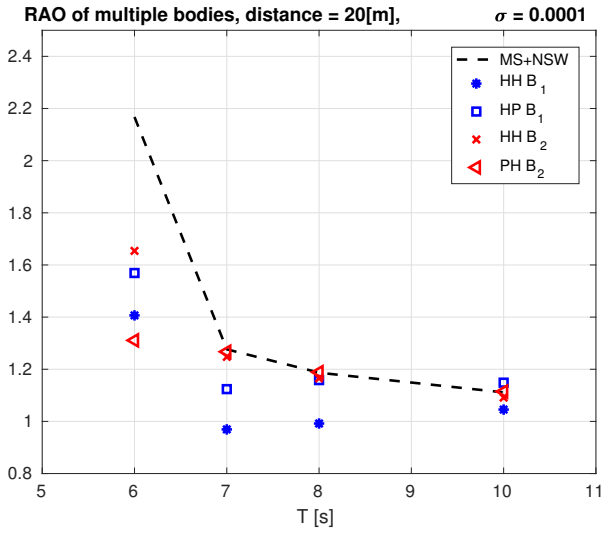

b

Figure 19: RAO plots for a stream wave of period $T = [6, 7, 8, 10]s$ and steepness $\sigma = 0.0001$ for the multiple bodies tests with the distance between the bodies dependent on the wave length $l = 2\lambda$ in figure a and for a fixed distance of 20 meters in b: the dashed line is the single body RAO, $*$ and $\times$ the first and second heaving bodies in series, $\square$ a heaving body in front of a pontoon and finally $\triangleleft$, a heaving body behind a pontoon.

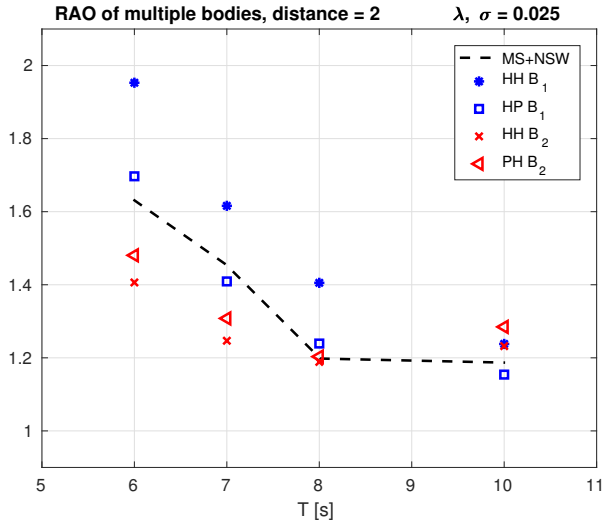

a

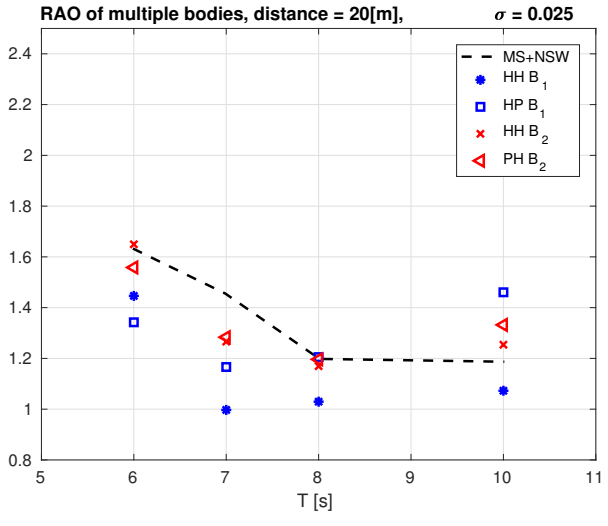

b

Figure 20: RAO plots for a stream wave of period $T = [6, 7, 8, 10]s$ and steepness $\sigma = 0.025$ for the multiple bodies tests with the distance between the bodies dependent on the wave length $l = 2\lambda$ in figure a and for a fixed distance of 20 meters in b: the dashed line is the single body RAO, $*$ and $\times$ the first and second heaving bodies in series, $\square$ a heaving body in front of a pontoon and finally $\triangleleft$, a heaving body behind a pontoon.